ELSEVIER

Sensors and Actuators B 61 (1999) 100–127

SENSORS AND ACTUATORS B CHEMICAL

www.elsevier.nl/locate/sensorb

Remote opto-chemical sensing with extreme sensitivity: design, fabrication and performance of a pigtailed integrated optical phase-modulated Mach–Zehnder interferometer system

R.G. Heideman [1], P.V. Lambeck [*]

MESA Research Institute, University of Twente, P.O. Box 217, 7500 AE Enschede, Netherlands

Received 6 April 1999; received in revised form 3 August 1999; accepted 6 August 1999

Abstract

This paper describes the design, fabrication and testing of a pigtailed integrated optical (IO) phase-modulated Mach–Zehnder interferometer (MZI) including both the optical chip and the electronics. The optical chip is realised in SiON technology. The IO components (the sensing function, the straight waveguiding channels, the phase modulator, the polariser, the splitter, the combiner and the fibre-to-chip connection unit) are individually optimised and interconnected by using transversal adiabatic tapers. To obtain a high waveguide evanescent field sensitivity, the sensor is designed for — but not limited to — a wavelength of 632.8 nm. The integrated MZI is actively phase-modulated by virtue of the electro-optic effect of the incorporated material zinc oxide (ZnO). The electro-optical voltage–length product V_π is $\sim$16 V cm at frequencies above $\sim$10 Hz. The polariser is a distributed function, that effectively filters TM-polarised light (TE/TM polarising ratio $>$30 dB). The fibre pigtail, affording remote optical sensing, is based on a cheap, easy-to-use fibre-to-chip connection with a typical coupling efficiency of 50%, while the device throughput (''insertion loss'') is ~ -20 dB. The drive- and demodulation electronics enable a phase resolution $5\times10^{-5}\times2\pi$, corresponding to a refractive index resolution of $\sim2\times10^{-8}$. The sensing system as has been realised up to now shows a phase resolution of $\sim1\times10^{-4}\times2\pi$, its long-term stability (hours) being $\leq3\times10^{-4}\times2\pi$. This corresponds to a refractive index resolution of $\sim5\times10^{-8}$, and a long-term stability of $\sim10^{-7}$.

Keywords: Opto-chemical sensor; Pigtailing; Remote; Zinc oxide (ZnO); Electro-optic; Phase modulation; Mach–Zehnder interferometer; Fibre-to-chip coupling; V-grooves; Silicon (Si); Silicon nitride (Si_3N_4); Silliliconoxynitride (SiON); Voltage–length product; V_π; Insertion loss

1. Introduction

There is a growing need for sensitive chemical sensors in areas such as process technology, health care, environmental control, biotechnology, etc. [1,2]. For many applications these sensors should show a high resolution over a wide dynamic range, they should be very sensitive, selective, fast, small and cheap, and should be suited for remote sensing. An attractive option fulfilling all these requirements is offered by integrated optical (IO) sensors [3]. In these optical chips the chemical parameter to be sensed, the measurand, influences in the sensing region directly or by means of a chemo-optical transduction layer the propagation properties of a guided light beam propagating through the chip. Using appropriate optical circuitry, these changes of propagation properties can be converted into a change of the optical output power. In turn, this is measured using a photo detector and appropriate electronics. Generally, selectivity is provided by the chemo-optical transduction layer, alternatively called the sensitive layer. This layer contains receptor units, that selectively associate with the chemical entities of the measurand. In addition, this layer can concentrate the measurand molecules and enhance the optical effects of their presence.

Using identical optical chips and electronics, the concentration of a large variety of measurands can be determined, simply by applying the appropriate transduction layer. Such sensor families can imply immunosensors having antibody proteins as receptor molecules [4], gas sensors (e.g., CO_2, SO_2) with silicates containing functional organic groups [5], etc.

[*] Corresponding author. Tel.: +31-53-489-2746; fax: +31-53-489-3343; e-mail: p.v.lambeck@el.utwente.nl

[1] Currently working at Meteo Instruments, Weltevreden 4c, 3731 AL de Bilt, Netherlands.

0925-4005/99/$ - see front matter
PII: S0925-4005(99)00283-X

Mostly the relevant changes of optical parameters occur in a region just outside the core layer of the waveguide, the evanescent field region (see Fig. 1). Hence, such chemical IO sensors are often called evanescent field sensors. The changing optical parameters imply whether the refractive index n, the absorption coefficient α, or luminescence parameters. In the refractive and absorptive sensors the parameter change expresses itself as a change of the (complex) phase velocity of the guided beam and can be quantitatively expressed as the change of the (complex) effective refraction index $\tilde{N}_{\text{eff}}$ of the propagating mode. A pure index change manifests itself as a change of the real part of the effective index, an absorption change as a change of its imaginary part. In the refractive sensors (purely Δn) the read out of the change ΔN_{eff} can be based on mode coupling, as is the case in surface plasmon resonance (SPR) sensors [6–8] and grating sensors [9,10], or on the related change of the phase. The latter form the base for the interferometric sensors such as the difference interferometer (polarimeter) [11,12] and the Mach–Zehnder Interferometer (MZI) [13–18].

For all these types of Δn-based sensors, the minimal detectable change of the effective refractive index ΔN_{eff} has been derived [3,19] to be:

$$\Delta N_{\text{eff,minimal}} = g(\lambda / L_{\text{int}}) \quad (1)$$

with L_{int} the ''interaction length'' of the guided wave with the analyte, λ is the wavelength used, and the factor g, depending on the applied experimental measurement techniques, is generally in the order of $1–5 \times 10^{-3}$ [3].

Although very good results are obtained with both the SPR sensor and the grating coupler concept, the interferometric sensors are generally supposed to have the highest sensitivity potential [3,17,19]. This is mainly based on the possibility of using large interaction length values resulting in enhanced sensitivity (see Eq. (1)). A typical value of L_{int} is 1 cm for the MZI, being (at least) an order of magnitude larger than the typical values of 1 mm for the grating coupler and 10–100 μm for the SPR sensor. Amongst the interferometric sensors it is only the MZI sensor that contains an easily accessible reference arm (see Fig. 2). When used properly, this reference arm can make the sensor (nearly) insensitive to many perturbing effects [19,20]. The resulting large intrinsic stability results in an improved sensor resolution, making the MZI sensor very attractive [4].

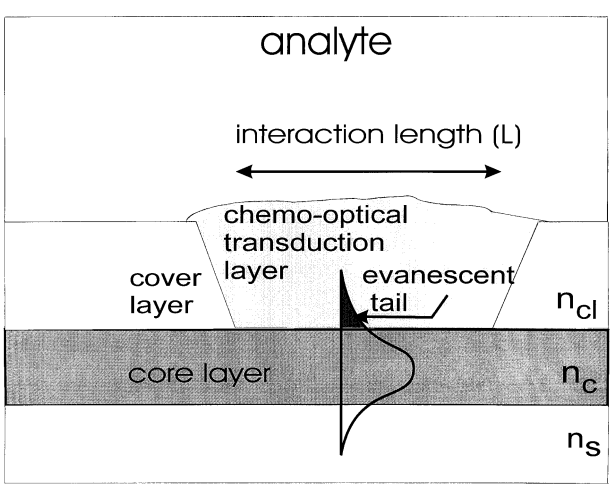

Fig. 1. Cross-section of a three-layer waveguide along the propagation direction of the light. The sensing region is filled with the chemo-optical transduction material of which the optical properties are probed by the evanescent tail of the modal field.

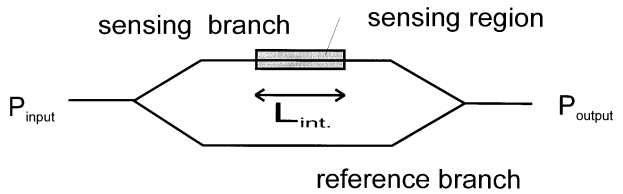

Fig. 2. Schematic top view of an IO MZI consisting of channel waveguides. The sensing branch contains the sensing region (grey).

The high potential of the integrated MZI has initiated a large amount of research. Recently much progress has been made, resulting in various promising applications [13–18,20–22]. Nevertheless, until now the IO MZI is seldom applied for commercial sensor applications. The reason may be, that coping with intrinsic factors, such as fringe order ambiguity, directional ambiguity and sensitivity fading, just as with extrinsic disturbing factors such as light source and temperature fluctuations and in addition the influence of technological imperfections, will lead to rather complicated optical chips and processing electronics.

In this paper, we will describe the design, the realisation and the performance of a complete MZI system, including both the optical chip and the electronics. The design objectives will not be directed to obeying a given set of quantitative specifications but will show a more qualitative nature, such as a low detection limit and a high resolution over a wide range. Also the system should be incorporated into a fibre network, hence amongst others a low input power is wished. The area of the optical chip has to be kept small, while there is a strong wish to keep the technology as simple as possible implying a small number of technological steps only.

An analysis of the MZI (Section 2) enables the transformation of the general objectives into more operational ones. A functional structure is proposed and requirements are set to the individual functions. In Section 3, a novel serrodyne type of modulation principle will be introduced. After a discussion of the choice of the materials and the (available) technologies (Section 4) the individual functions are designed, optimising them with respect to their requirements (Section 5). In Section 6 the separate steps

for the fabrication of the optical chip are given. Both the individual components and the complete sensing system are tested and the results are discussed (Section 7). Finally the prospects of this new device are given (Section 8), followed by a summary of the main conclusions (Section 9).

2. MZI analysis

2.1. The principle

In a MZI (see Fig. 2), the incoming light is divided over two branches. Both branches are combined again, that combination leading to the interference of the individual branch beams. This results into an output power P_{out} that depends on the phase difference $\Delta\varphi_b$ of both beams in the combination area. It is that phase difference that will be made dependent on the measurand concentration.

2.2. Conversion of a chemical concentration into a phase difference

A cross-section of the sensing waveguide along the propagation direction has been given in Fig. 1. In that waveguide, the light can propagate in the form of some specific modes only: lateral patterns of the electric field (field profiles), each pattern being related to a specific value of the phase velocity and hence to a specific value of the effective index N_{eff}. The number of modes able to propagate through the waveguide, their corresponding N_{eff}-values and their field profiles depend strongly on the refractive index distribution in a cross-sectional plane perpendicular to the propagation direction. Mono-modal waveguides are possible. To make the propagation insensitive to environmental conditions, the waveguide core layer is sandwiched between a cladding layer and a substrate layer (see Fig. 1). Both layers have such a thickness, that the field profile is completely confined within that three-layer waveguiding system. To sense however, the cladding layer has to be locally removed (the sensing region) and there the mode propagation will be sensitive to the refractive index changes of the materials within the evanescent field region.

Here two cases have to be distinguished.

- In the first case the evanescent field region is completely filled with one sensitive material only (homogeneous sensing). This material can be a liquid, e.g., a mixture of two liquids or a solution of one chemical compound, the refractive index being a measure for the mixing ratio or the concentration ([c]), respectively. It also can be a solid in which (selective) receptor sites are incorporated, its refraction index being a measure for the fraction of filled sites.
- In the second case a very thin chemo-optical transduction layer has been applied within the evanescent field region directly on top of the core layer (surface sensing). The evanescent field is extending into the environment above that layer too. This is, e.g., the case in immune sensors, where the transduction layer is formed as a mono-layer of antibodies. Here N_{eff} is sensitive to changes of the refractive index in both the transduction layer and the environment.

In the sensing part the refractive index change within the evanescent field region (due to the measurand) results into a change of the effective index ΔN_{eff} and hence into a phase change $\Delta\varphi_{m(easurand)}$:

$$\Delta\varphi_m = \frac{2\pi}{\lambda_0} L_{int} \Delta N_{eff} \quad (2)$$

where λ_0 is the vacuum wavelength of the light used, L_{int} is the interaction length.

The phase difference will be the larger with larger ΔN_{eff} and L_{int} and with smaller wavelength λ_0. The available chip area limits the interaction length.

2.3. Conversion of the phase change into a power change

2.3.1. Perfect technology

At first, a hypothetical MZI will be considered that is produced by a perfect technology, enabling to produce exactly the device as is intended. This perfectness implies, e.g., that the ratio of the beam powers in both branches is exactly one, and the phase difference in absence of the measurand is exactly zero. We also assume the light source to be strictly monochromatic. It can be derived [23] that the output power P_{out} can be given as:

$$P_{out} = \sum_k P_{in,k}(1 + \cos\Delta\varphi_{m,k}) \quad (3)$$

where $P_{in,k}$ is the input power of the k-th mode, $\Delta\varphi_{m,k}$ is the measurand-induced phase difference related to mode k.

For the case that only one mode is propagating, the transfer function of the MZI, i.e., the power ratio P_{out}/P_{in}, is depicted as a function of $\Delta\varphi_m$ in Fig. 3. The points where $\Delta\varphi_m = (n + 1/2)\pi$ are called the quadrature points. From this power ratio the phase difference $\Delta\varphi_m$ has to be derived. This implies that in addition to P_{out} also P_{in} has to be measured. This can be realised by tapping off a small and constant part of the input power and leading this to another detector.

The transfer function is periodical, one period being called a fringe. Fig. 3 clearly illustrates the three intrinsic problems related to the MZI principle.

- The fringe order ambiguity: in determining the phase difference from a given value of the power ratio in addition to $\Delta\varphi_m$ every $\Delta\varphi'_m = \Delta\varphi_m + k2\pi$, with k, being an integer, is an equally probable solution.
- The directional ambiguity: within a fringe starting from an extremum in the transfer function the direction of the change of $\Delta\varphi_m$ cannot be deduced from the transfer function change only.

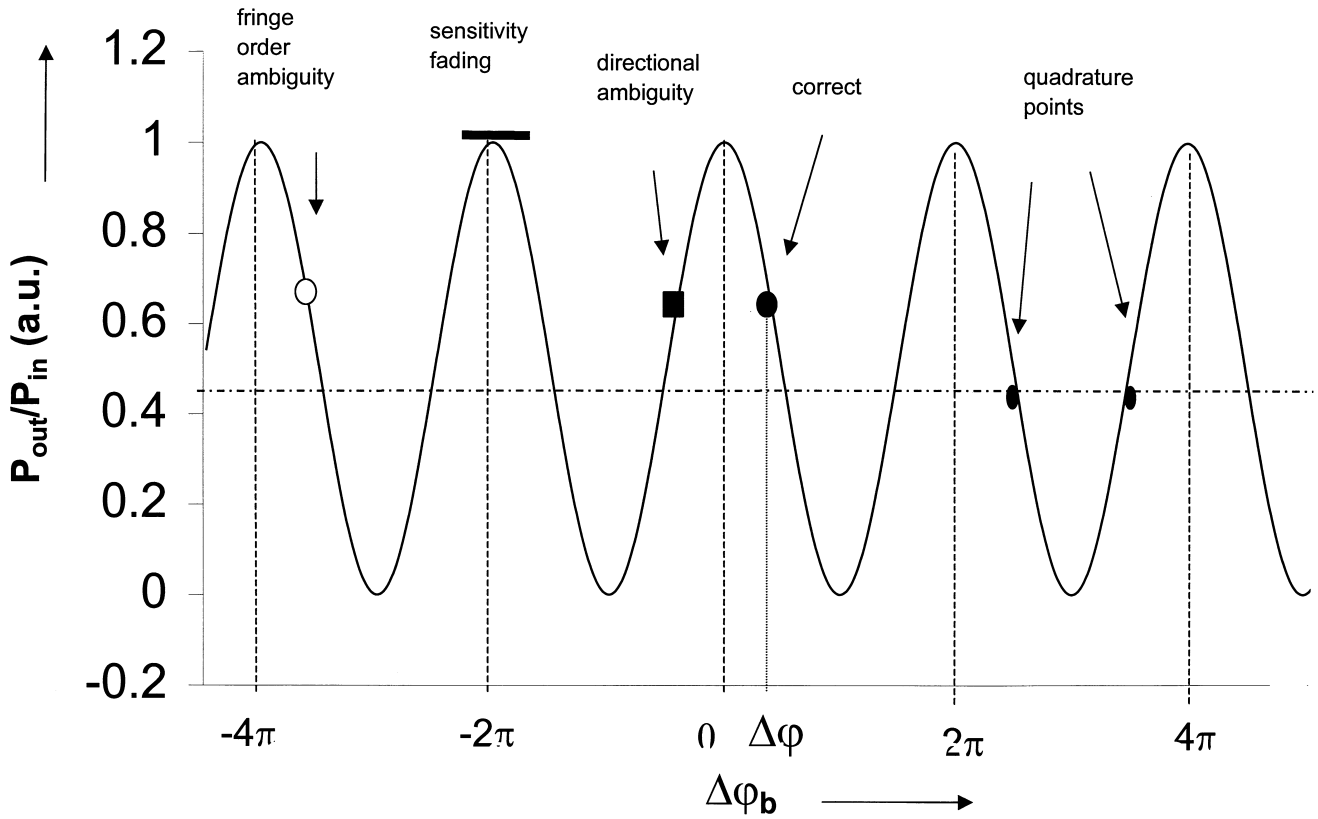

Fig. 3. Plot of the transfer function of the MZI versus the phase difference $\Delta\varphi_b$, showing the fringe pattern and the associated intrinsic problems for the determination of $\Delta\varphi_m$ from a measured transfer function value.

· The sensitivity fading: the sensitivity (e.g., the slope of the fringe pattern) is dependent on the value of $\Delta\varphi_m$, becoming even zero at the extremes of the transfer function.

Using perfect technology a solution might be found in adjusting $\Delta\varphi_b$ at $\Delta\varphi_m = 0$ $(\equiv \Delta\varphi_{b,\,[c]=0} \equiv \Delta\varphi_0)$ to a quadrature point and to lower the interaction length to a value where all possible $\Delta\varphi_m$ changes are limited to a quarter of a fringe. This however will be at cost of the resolution and the detection limit.

A more promising way is to apply active phase modulation, which overcomes the problems of directional ambiguity and sensitivity fading. In Section 3, a new phase modulation principle will be presented, that also affords for counting the fringes in an easy way.

Propagation of several modes at a time will complicate the measurements remarkably. Hence, in general, the MZI is designed as a mono-modal system which, in spite of the epithet mono-modal, has two modes (the TE_0 and the TM_0) having their electric and magnetic field vectors, respectively, parallel to the layer boundaries, which can propagate. Both modes have non-identical field profiles and (in general) also non-identical N_{eff}-values, hence in the MZI they will behave in a different way. Now, there are several options to proceed.

· One can launch one mode only (either TE or TM) and then Fig. 3 holds.

· In case both modes are launched at the same time, the separate input and output powers can be determined by introducing appropriate filter functions, appealing on the difference in N_{eff} or field profiles of both modes [24]. This is in fact a variation of the well-known dual wavelength interferometry [25], in principle, enabling the determination of the fringe number.

· If launched from a common single-mode fibre, where, in general, the polarisation state of the mode at the fibre output is unknown, the power ratio of the launched TE_0 and TM_0 modes will be unknown. In case one desires one-mode propagation only, the other mode has to be removed, e.g., by implementing a TE/TM polariser. To exclude the chance that all launched light will be in the wrong polarisation state, either a non-polarised laser or a smart polarisation converter has to be applied; such a device is subject of current research within our group.

2.3.2. Imperfect technology

A lot of on-chip technological imperfections (non-uniformity of the thickness, width and losses of the waveguide, imperfect splitter and combiner functions, sensor window-induced losses, etc.) result into deviations from

relation (2), which can be represented by introducing the so-called fringe visibility V together with a bias phase-offset $\Delta\varphi_0$ [23]:

$$P_{\text{out}} \sim P_{\text{in}}\left(1 + V\cos\left(\Delta\varphi_{\text{m}} + \Delta\varphi_0\right)\right) \tag{3a}$$

where $\Delta\varphi_{\text{m}} + \Delta\varphi_0 = \Delta\varphi_{\text{b}}$, and $0 \le V \le 1$.

The phase offset $\Delta\varphi_0$ now represents the optical path length difference between the arms of the MZI in absence of the measurand:

$$\Delta\varphi_0 = \int_{A,\text{branch 1}}^{B} N_{\text{eff}}(l)\,\mathrm{d}l - \int_{A,\text{branch 2}}^{B} N_{\text{eff}}(l)\,\mathrm{d}l \tag{3b}$$

where A and B correspond to the splitting and combining point, respectively (see Fig. 2).

From the power ratio $P_{\text{out}}/P_{\text{in}}$, $\Delta\varphi_{\text{m}}$ can be deduced only if V and $\Delta\varphi_0$ are known from calibration.

Obviously V weights the effects of a phase change on the transfer function and for obtaining a high resolution V has to be close to unity. This means that imperfections have to be reduced as much as possible. The V-value is also related to the non-monochromatism of the light source expressed as the spectral band width Δf_{FWHM}, which can be can be easily quantified for laser diodes [23] as being:

$$V = V_0 \exp\left(\frac{\Delta f_{\text{FWHM}}\,\Delta\varphi_{\text{b}}}{2 f_0}\right) \tag{4}$$

where V_0 is the fringe visibility for a monochromatic light source with frequency f_0.

In order to fulfil the wish of having V close to unity the unbalance $\Delta\varphi_{\text{b}}$ has to be low. Hence, for reducing effects of spectral band width a well-balanced (i.e., both branches as identical as possible) MZI is required. This points to the implementation of a sensing window not only in the sensing branch, but also in the reference branch, the latter being filled with a passive material with a refractive index and — in case of surface sensing — also a layer thickness as near as possible to that of the sensitive material.

2.4. Noise influences

Noise is generated both by the light source and the detector. Effects of noise in the driving current of the source in general can be reduced strongly by using well-balanced MZIs. Effects of laser shot noise and spectral band width can be expressed as uncertainties in the phase difference. In case the MZI is (held) in a quadrature point, as will be done using the phase modulation method proposed in Section 3, the exact expressions become [23]:

$$\sqrt{\langle \Delta\varphi_{\text{shot}}^2 \rangle} = \frac{1}{V}\sqrt{\frac{2hf_0\Delta f_{\text{det}}}{P}} \tag{5a}$$

$$\sqrt{\langle \Delta\varphi_{\text{spectr}}^2 \rangle} = 2\frac{\tau}{\sqrt{t_{\text{c}}}}\sqrt{\Delta f_{\text{det}}} \tag{5b}$$

where P is the power emitted by the light source, τ is the delay time, i.e., the difference in time needed for propagation along both branches, t_{c} is the coherence time, Δf_{det} is the detection band width.

From the relations it can be seen that, also for reducing the noise, the V factor has to be close to unity and the MZI has to be well-balanced ($\tau \to 0$). Both phase errors are proportional to the square root of the detection band width, so this band width has to be made as small as possible. To obtain a spectral band width related phase error smaller then $2\pi \times 10^{-5}$ over a wide range, a laser has to be used as the light source [23]. Because gas lasers are much less sensitive to temperature fluctuations and to reflected light then laser diodes, gas lasers are preferred.

As to the detector noise: if the smallest detectable phase step (the resolution) is equivalent to a power difference ΔP, then the ratio of ΔP and the NEP (noise equivalent power) of the detector has to be larger than about three. Because of the sinusoidal periodicity of the transfer function, ΔP will depend on $\Delta\varphi_{\text{b}}$. To obtain a phase resolution of $2\pi \times 10^{-5}$ near the quadrature point, $\Delta P/P_{2\pi}$ has to be smaller than 5×10^{-6}, where $P_{2\pi}$ is the power on the detector in case $\Delta\varphi_{\text{b}} = m2\pi$, m being an integer. $P_{2\pi}$ is related to the power emitted by the light source P_{source} by:

$$P_{2\pi} = P_{\text{source}}\eta_{\text{source-chip}}\eta_{\text{chip}}\eta_{\text{chip-detector}}, \tag{6a}$$

where $\eta_{\text{source-chip}}$ and $\eta_{\text{chip-detector}}$ are the efficiencies of coupling light from the source into the chip and from the chip into the detector, respectively, and η_{chip} indicates the transfer function for $\Delta\varphi_{\text{b}} = m2\pi$, this value being larger with smaller propagation losses of the MZI.

Because the sensor has to be incorporated into a fibre network, the laser has to be connected to a fibre: therefore, $\eta_{\text{source-chip}} = \eta_{\text{source-fibre}}\eta_{\text{fibre-chip}}$. To obtain a resolution better than $1 \times 10^{-5} \times 2\pi$, one has to obey the relation:

$$P_{2\pi} \ge \frac{\Delta P}{5 \times 10^{-6}} \ge \frac{3NEP}{5 \times 10^{-6}}, \text{ thus} \tag{6b}$$

$$P_{\text{source}}\eta_{\text{source-fibre}}\eta_{\text{fibre-chip}}\eta_{\text{chip}}\eta_{\text{chip-fibre}}\eta_{\text{fibre-detector}} > 6 \times 10^5 \text{ NEP (at } \Delta\varphi_{\text{b}} = m2\pi) \tag{6c}$$

To feed many sensor chips from one laser source, the required P_{source} has to be as small as possible, meaning that

- all coupling efficiencies has to be high; for this reason, at the input a single-mode fibre and at the output a high NA multi-modal fibre will be used;
- the propagation losses of the MZI have to be small;
- the NEP of the photodiode has to be small, in combination with:
- the detector band width has to be small.

2.5. Temperature fluctuations

The influence of temperature fluctuations on the read-out system is small, because both branches of the MZI can be close (distance about 40 μm) to each other. To minimise

the temperature difference between both branches a substrate with a high thermal conductivity (such as a silicon wafer) is preferred. The effect of temperature on the association constants of the receptor units in the sensitive layer cannot be compensated for; hereto, temperature stabilisation- or software-based corrections after measuring the real temperature are needed. Influence of temperature on the refractive index of the sensitive layer (empty sites) and of the environment (in case of surface sensing) will also influence $\Delta\varphi_b$. This can be compensated for by applying a comparable sensing window in the reference branch. Here, this window should be provided with a passive layer with parameters (thickness, refractive index and temperature coefficient of the refractive index), nearly identical to those of the sensitive layer, e.g., a passivated sensitive layer. In case of homogeneous sensing this passivation can be obtained by simply covering the layer with an additional layer that should be impermeable for the measurand molecules.

2.6. Conclusions

The given analysis enables a conversion of the original system objectives into more device or component oriented goals and into boundary conditions.

(1) Functions for dynamic modulation have to be implemented on the chip.

(2) In addition to the sensing window in the signal branch, an identical window has to be implemented in the reference branch. This window has to be filled with an inactive layer, having an identical layer thickness, refractive index and temperature coefficient of the refractive index as the sensitive material in the sensing window.

(3) TM- or TE-polarised light has to be detected only, hence a TE/TM polariser has to be added at the chip.

(4) From the fibre the light has to be coupled efficiently into the chip, requiring the implementation of a fibre–chip coupling function.

(5) A function has to be implemented to tap off a constant part of the input power.

(6) Electronics for modulation and demodulation has to be added.

(7) The waveguide channels have to be mono-modal.

(8) The MZI has to be well-balanced, or (alternatively) the fringe visibility has to be close to unity. This means that the optical path length and the losses in both branches have to be nearly identical. Also the splitting and combining functions, the latter being the inverse of the first one, have to show a splitting ratio close to unity. To obey the balancing condition it should be nice to apply modulators in both branches, being driven in counter-phase. This can be realised by using two identical electro-optical modulators. Here Δn_{e-o} is proportional to the electrical field E and so to the applied voltage. Besides, electro-optical modulation requires low energy consumption and does not produce excess heat, which could disturb the detection process. To become compatible with standard electronics, the driving voltage has to be low, preferentially not exceeding the 5-V level.

(9) Propagation losses of the MZI have to be small.

(10) Light source and detector have to show a low noise level. Here a small detection band width is favourable.

(11) The spectral band width of the light source has to be small, just as the wavelength, favouring the use of a gas laser.

(12) A substrate material with a high thermal conductivity is preferred.

(13) Calibrations are required for determining the values of the fringe visibility V and the phase offset $\Delta\varphi_0$.

All these requirements result into a functional structure as depicted in Fig. 4.

In the previous sections, the theoretical sensitivity considerations on an IO MZI-sensor have led to several important choices and recommendations. In Fig. 4, those choices have been summarised. From this functional structure analysis, the difficulties for commercial exploitation

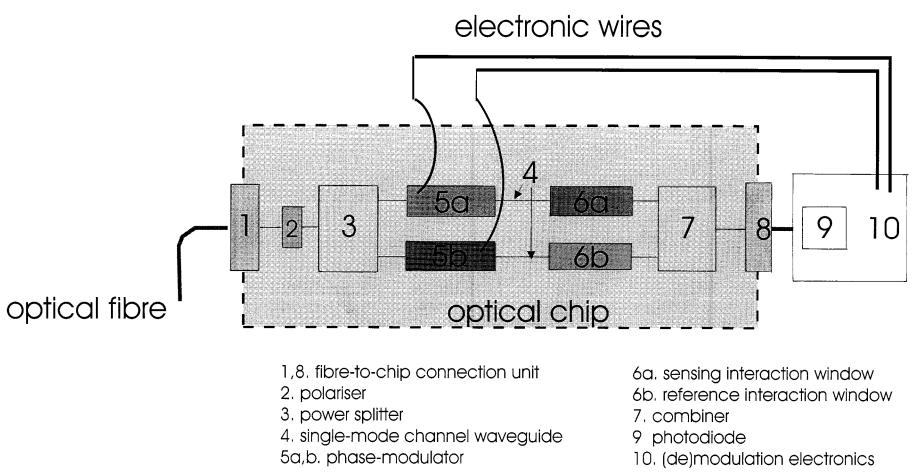

Fig. 4. Functional structure of an IO phase-modulated MZI sensing system. For an explanation of the optical components, see text.

of IO MZI sensor systems can be understood: the MZI should be actively phase (de)modulated, requiring elaborate external electronics. Besides, the optical chip should consist of single-mode optical channels supporting five main functions, being:

- splitters and combiners;
- sensing regions;
- optical phase modulators;
- a polariser;
- fibre-to-chip connection units.

Optimal performance of all these main functions will put different and — as can be expected — sometimes contradictory conditions to the waveguide structure.

3. (De)modulation principle

In Section 2, it has been concluded to apply an AC modulation scheme and to implement an electro-optic modulator in each of both interferometer branches. Many modulation principles are known to increase the sensitivity of the integrated interferometer [22,23]. A survey of the most relevant ones in case of electro-optical phase modulation has been given in Ref. [23]. Here we propose a novel serrodyne type of modulation method based on the detection of quadrature points. The principle is visualised in Fig. 5. In Fig. 5a the time dependence of the triangular modulating voltage V_Λ is shown, being the sum of absolute

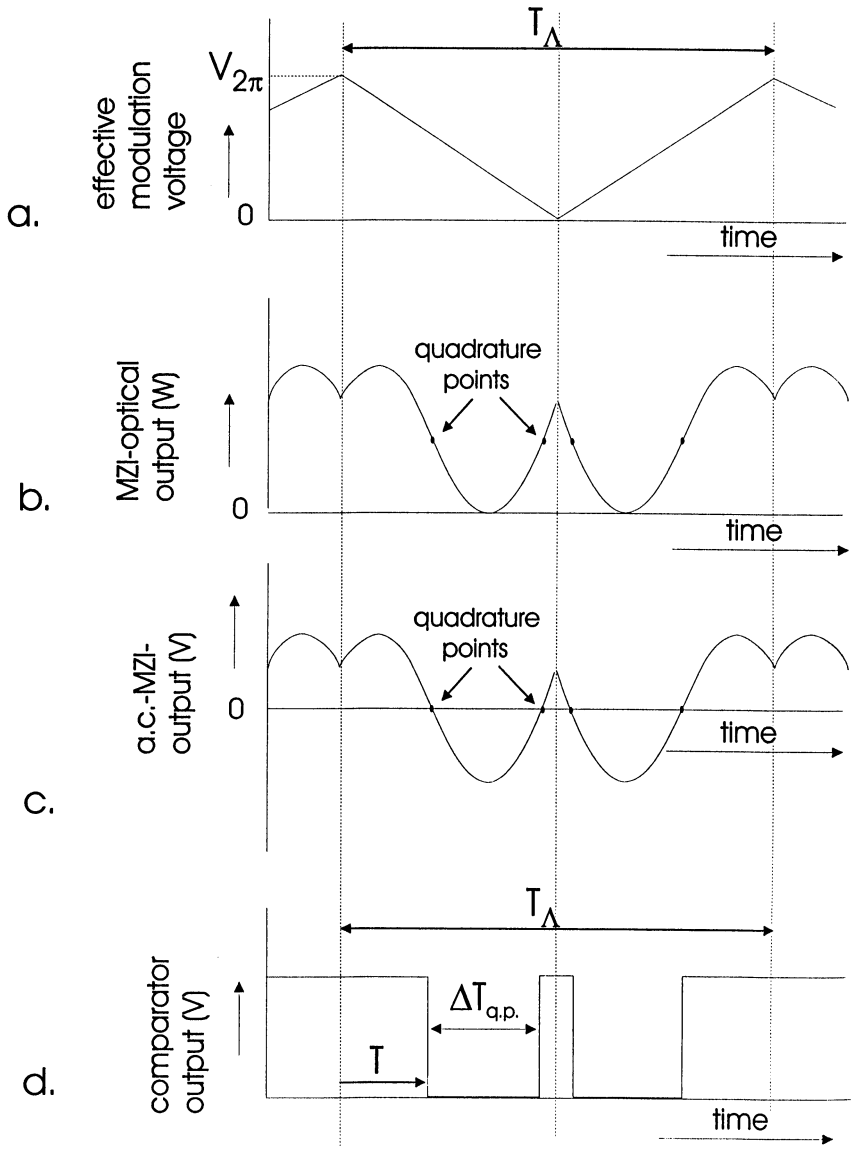

Fig. 5. Schematic representation of the active phase modulation used: the time triangular-shaped voltage with amplitude $V_{2\pi}$ and period T_Λ (a) results into a time-dependent MZI output (b). With an appropriate RC network this response is AC-coupled (c), and digitised to standard TTL level using a ''zero-level'' comparator (d).

values of the voltages as applied to the individual electrodes. The maximum voltage has to correspond to an induced phase difference $\Delta\varphi_{e-o}$ exactly equal to 2π; this voltage is called $V_{2\pi}$. Using a modulation voltage with $V_{2\pi}$ as top-to-top value in every half cycle, the quadrature points will be passed two times (see Fig. 5b). Using this modulation voltage, the average value of the transfer function will become independent on the specific value of the measurand-induced phase difference $\Delta\varphi_m$. This is very important, because after filtering out the DC component by an appropriate RC network, the zero points of the remaining output voltage always coincide with the quadrature points (see Fig. 5c). With a zero-crossing comparator this response is digitised to standard TTL-level (see Fig. 5d).

The value of $\Delta\varphi_m$ can be obtained easily from Fig. 5d according to:

$$\Delta\varphi = \Delta\varphi_m + \Delta\varphi_0 = \left(\frac{T}{T_\Lambda}\right)4\pi + N2\pi, \tag{7}$$

where T_Λ is the period of the triangular modulation voltage, N is the fringe number and $\Delta\varphi_0$ is the phase offset.

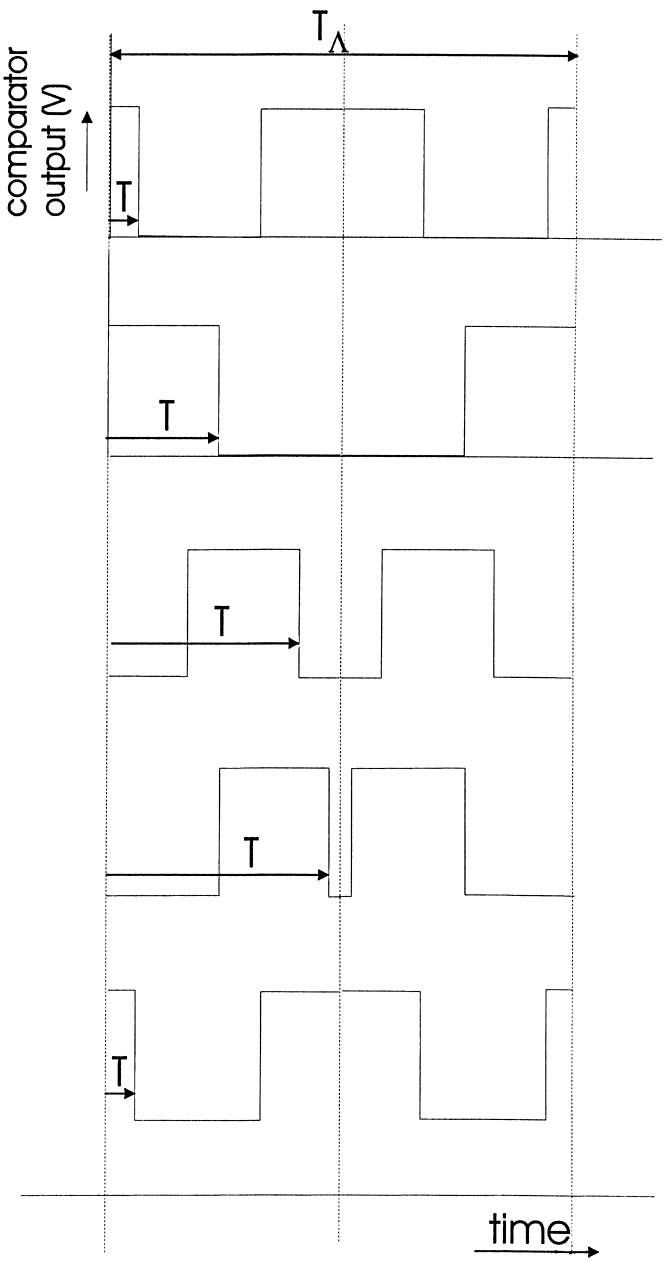

Fig. 6. The passing of a fringe is registered for by an abrupt change in the value of T, this change having a magnitude of $\sim 1/2T_\Lambda$, its sign determining fringe number increase/decrease.

The fringe number is determined by counting how many times a fringe has been passed since the last ''measurand is zero'' state. The passing of a fringe is recognised from an abrupt change in the value of T (see Fig. 6), this change having a magnitude of $1/2T_\Lambda$. The sign of the change determines the direction of the fringe passing. This principle solves both the fringe ambiguity problem and the sensitivity fading, as within a fringe $\Delta\varphi$ is linear with the time interval T. The principle also shows additional advantages.

– Only for $V_\Lambda = V_{2\pi}$ the time interval $\Delta T_{\text{q.p.}}$ (see Fig. 5) is exactly equal to $1/4T_\Lambda$, giving a criterium for adjusting V with the aid of a feedback loop.

– The zero crossings position is independent on the amplitude of the output voltage (Fig. 5c). So these positions are influenced neither by the specific value of the fringe visibility V nor by the specific value and low frequent intensity fluctuations of the light source. Hence, the requirement of obtaining the exact values of both the input power (using the tap-off) and the fringe visibility (by calibration) can be cancelled. However, for obtaining high resolution it remains relevant to maintain the requirement of V being close to unity.

The output signal is periodic, with a period T_Λ; within a period the signal varies sinusoidally with a frequency $2/T_\Lambda$. In order to have a small detection band width, T_Λ has to be large. It is clear that the value of the period T_Λ also limits the maximum speed of the refractive index changes that can be measured: the smaller T_Λ, the higher that speed. More quantitative statements are strongly related to the specific properties of the electronics applied and shall not be treated here.

4. Materials and technology

To realise the passive IO circuits, the SiON technology, as developed in our laboratory [26], is well-suited. By varying the O/N ratio the refractive index can be set between $n = 1.46$ (SiO_2) and 2.01 (Si_3N_4). The specific value is controlled by the gas flow ratios, when depositing these layers by low-pressure chemical vapour deposition (LPCVD) or plasma-enhanced chemical vapour deposition (PECVD) technologies. The waveguiding multi-layer structure (see Fig. 1) commonly consists of a SiO_2 substrate layer, a SiON core layer and a SiO_2 cladding layer and will be deposited on a silicon wafer, being a well-suited substrate material amongst others because of its high thermal conductivity. The Si wafer also offers the possibility of being provided with V-grooves for the fibre–chip coupling [27–32]. These multi-layer stacks have to be laterally patterned for defining the channel structure and therefore the optical circuitry. For that, photolithography and dry and wet etching methods are available. The relevant data concerning our technology are given in Table 1.

An attractive silicon compatible material allowing electro-optical phase modulation is zinc oxide (ZnO) [18,33–35]. As ZnO can withstand temperatures up to 350°C without degradation of its (electro)optical characteristics [34], it enables its shielding to environmental influences using a passivation layer of PECVD SiO_2. When used in an optical waveguide geometry, it shows reasonable low attenuation values (1–3 dB/cm for $\lambda \geq 600$ nm, [34]) in combination with attractive voltage–length products (V_π), being typically 25 V cm [18]. The preferred deposition technique, sputtering [34], results into a polycrystalline columnar structure of thin ZnO films, with a homogeneous preferential polar axis orientation perpendicular to the substrate surface [34,35]. As only an electric field in the direction of this axis will result in macroscopic electro-optic effects, the top–bottom electrode configuration has to be applied (see Figs. 10 and 14), enabling the use of two electro-optical coefficients: the $r_{13} - (1.4 \times 10^{-12}$ m/V) coefficient for TE-polarised light, or the r_{33} coefficient (2.6×10^{-12} m/V) for TM-polarised light [36].

It has to be noticed that the ZnO film structure is known to have hardly any resistance to almost every liquid [37], hence special care has to be taken when fabricating both the modulator and the sensor interaction windows (see Section 6) [18].

5. Design of the individual functions

5.1. Introduction

In a first stage, the design of the individual functions optimised to the requirements will be presented. That concerns the waveguiding channels, the splitting and combining functions, the sensing function, the TE/TM po-

Table 1
Materials properties

Parameter	LPCVD Si_3N_4	PECVD SiON
Maximum thickness (nm)	500	~ 5000
Thickness non-uniformity δd over 5×5 cm (%)	1.5–2.0	< 1
Refractive index non-uniformity Δn over 5×5 cm	$2–5 \times 10^{-4}$	$2–6 \times 10^{-4}$
Reproducibility of thickness (%)	1	1–3
Reproducibility of refractive index	5×10^{-4}	6×10^{-4}
Optical loss at $\lambda = 632.8$ nm (dB/cm)	< 0.2 (as deposited)	< 0.2 (as deposited)

lariser, the modulator, and the fibre-to-chip coupling unit. For all calculations we will rely on well-established software, e.g., for calculating N_{eff}-values and field profiles of the modes of a multi-layer stack the ATR program and for calculating the beam propagation through an optical circuit the FDBPM method of the Prometheus program [38]. The optimal layer structures for the individual compounds will be compared and a strategy for coping with contradictional requirements will be presented and worked out. Finally the design of the electronics will be treated shortly. Because for all components the optimisation is strongly dependent on the used optical wavelength we will start with discussing the choice of the used wavelength and therefore the light source.

5.2. The light source

To have an efficient ΔN_{eff}-to-$\Delta\varphi$ conversion, the wavelength has to be small, as was concluded in Section 2.2. The requirement of having low propagation losses limits the wavelength to the transmission windows of the applied materials. Reduction of scatter losses asks for a large wavelength: due to the scatter losses in ZnO the minimal wavelength is limited to about 600 nm. To reduce the noise related to the spectral band width a laser should be used. Because of its smaller sensitivity to temperature changes and back reflection, a gas laser is preferred over a solid state laser. Considering all this, a He–Ne laser ($\lambda = 632.8$ nm) has been chosen, the common type having 5 mW emission power.

5.3. The waveguiding layer structure

The waveguiding layer structure, the slab guide, has to be mono-modal and for light transport the field profile has to be well-confined within this slab guide in order to avoid any influence of the environment. For example, the substrate layer has to be sufficiently thick to obtain negligible power leakage into the silicon wafer. From technological point of view it is advantageous to have a thin layer packet. Together this means that the index contrasts between the core layer and both other layers have to be large. Hence, the layer stack SiO_2–Si_3N_4–SiO_2 is well-suited. For a mono-modal layer, the minimal thickness of the substrate layer to have allowable leakage losses (≤ 0.01 dB/cm at 632.8 nm wavelength) has been calculated as a function of the core layer thickness (see Fig. 7). It is seen that for the TM_0 mode the required thickness is much higher then for the TE_0 mode. This suggests the possibility to remove the TM_0 mode simply by exploiting its power leakage into the silicon. To get an impression of the effects, the TM_0 losses are calculated as a function of the core layer thickness t_c, the substrate layer having a thickness value corresponding to a TE_0 loss of 0.01 dB/cm for every t_c-value (see Fig. 8).

From Fig. 8, it can be concluded that maximal TM_0 rejection can be obtained at $t_c = 60 \pm 10$ nm. For convenience, a value of 70 nm is chosen, as it goes with minimal SiO_2 thickness of only 1.32 μm. This combination yields a TM rejection of ~ 5.5 dB/cm, yielding a distributed polariser action of ~ 22 dB at a channel length of 4 cm. It

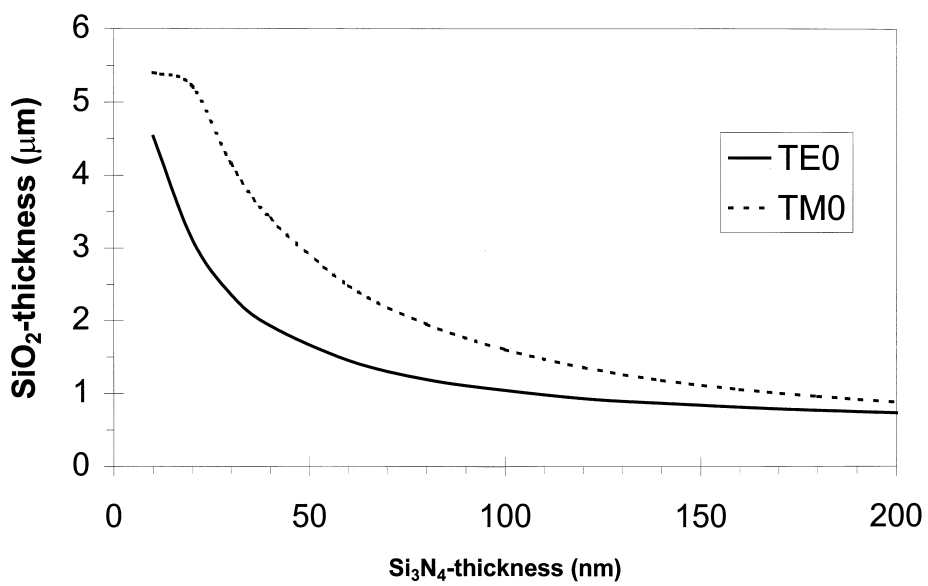

Fig. 7. Relation between the core layer thickness (Si_3N_4) and the buffer layer thickness (SiO_2), required for having a Si-related attenuation of 0.01 dB/cm for the TE_0 (———) and TM_0 (-----) modes.

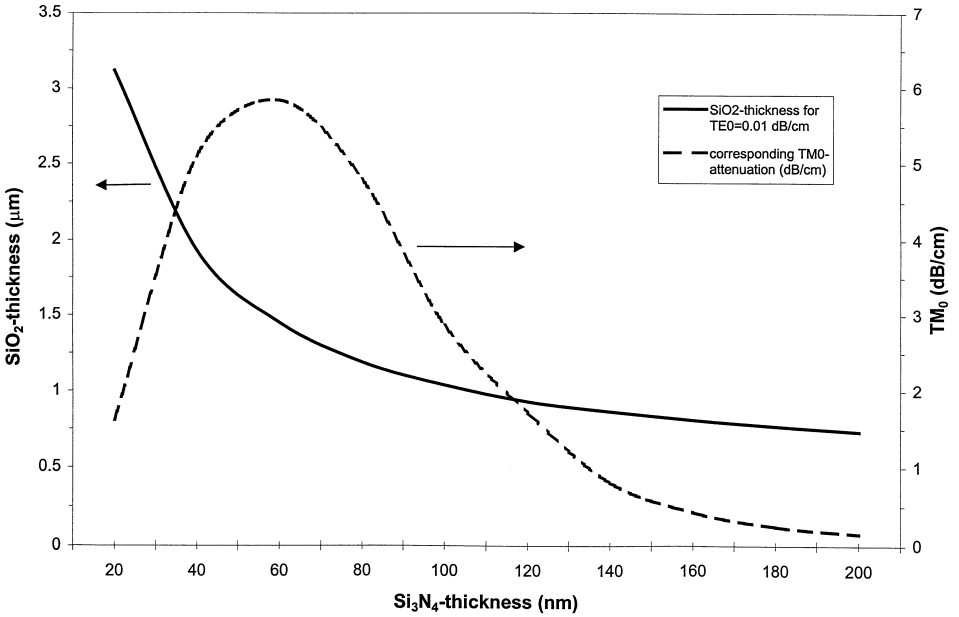

Fig. 8. The TM_0 attenuation as a function of the Si_3N_4 thickness for each value of that Si_3N_4 core layer thickness (-----), using the SiO_2thickness value as required for 0.01 dB/cm TE_0 attenuation (———).

should be noted that this TE/TM polariser action can be strongly improved — at the cost of an increased TE_0 attenuation — by a small reduction of the SiO_2 layer thickness. For example, the combination $t_c = 70$ nm, $t_s =$ 1.25 μm yields ~8 dB/cm TM_0 attenuation, at a TE_0 attenuation value of 0.018 dB/cm. In practice, the latter combination will be used.

5.4. The sensing unit

In the sensing unit the core layer will be in intimate contact with the sensitive material, being either a gas (seldom), a liquid or a solid. One of the objectives is to have a high sensitivity, meaning that $\partial N_{\text{eff}}/\partial n_{\text{sm}}$ has to be high, n_{sm} being the changing refractive index of the sensitive material (e.g., the chemo-optical transduction layer). Physically this is in line with saying that the fraction of the mode power propagating through the sensitive layer has to be as high as possible. In addition the core layer has to be resistant to any attack from the outside: it has to be chemically stable and also liquids are not allowed to diffuse from the environment into the core layer. The latter especially favours the use of LPCVD Si_3N_4 because of the absence of pores and pinholes.

The quantitative elaboration of the high sensitivity requirement depends on the type of mode propagating through the waveguide (in our case a TE_0 mode at $\lambda =$ 632.8 nm) and the refractive index distribution within the evanescent field region of this mode in the sensing unit. The latter leads to two extremes, being the homogeneous sensing (only one material in that region) and the surface sensing (a very thin sensitive layer on top of the core layer). In case of the used ''three-layer'' slab guide, the sensitivity as a function of normalised parameters for both extremes is given by the charts presented in [39]. For surface sensing, the sensitivity is increasing with a larger refractive index of the core layer. Hence, again from the SiON materials, Si_3N_4 is the best choice for the core material. This is also a proper choice for homogeneous sensing. For surface sensing, most often being restricted to biochemical reactions in a watery environment ($n_{\text{water}} \sim$ 1.33), the optimal Si_3N_4 thickness can be calculated to be ~75 nm.

For homogeneous sensing, the optimal core layer thickness strongly depends on the refractive index of the sensitive material. Assuming the substrate layer consists of SiO_2, from the charts [39], the optimal thickness can be obtained for various sensitive materials (see Table 2). It should be noted, however, that for $n_{\text{sm}} > n_{\text{substrate}}$ (being 1.457), the optimal thickness is the cut-off thickness. As in these situations, the evanescent field expands infinitely in the sensing material, this layer should be extremely thick. From practical point of view, this situation is therefore avoided.

Table 2
Optimal Si_3N_4 thickness for different materials in case of homogeneous evanescent field sensing*

	Watery gel ($n_{\text{sm}} \sim 1.35$)	Gelatine ($n_{\text{sm}} \sim 1.5$)	Polyimid (n ~ 1.6)
Optimal Si_3N_4 thickness (nm)	~75	~30	~45

*As calculated from Ref. [39].

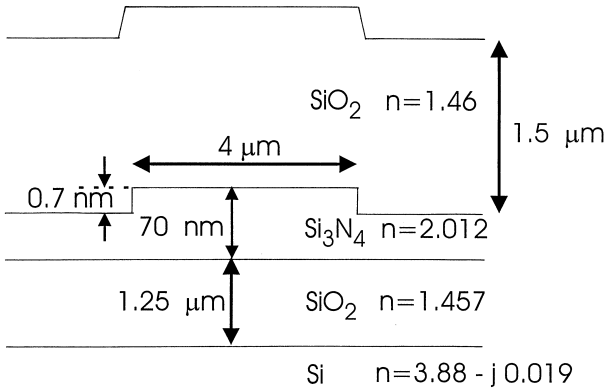

Fig. 9. Cross-section (perpendicular to the propagation direction) of the transport waveguide channel.

From the analysis given in Ref. [39] it follows, that for systems in between homogeneous and surface sensing, high sensitivities also require a thin (typical thickness about 100 nm) core layer with a high refractive index, while the sensitivity decreases with the wavelength of the light applied. In our sensor system, we will choose the core layer thickness to be 70 nm.

5.5. Definition of the waveguiding channels

The channels in the slab guide will be structured as mono-modal ridge type channels (see Fig. 9), the ridge being applied in the core layer. Accepting a mask generator defined minimum channel width of 4 μm, the ridge height is in the order of magnitude of nanometers. The exact value depends upon the material on top of the core layer, being SiO_2 in the transport guides and ZnO or the sensing material in the modulator and sensing function, respectively.

In order to have a small influence of temperature gradients both interferometer branches have to be close together. The minimum distance is determined by the evanescent field tails (defined as the $1/e$-value of the field at the channel boundary) of both channel modes, where the overlap has to be negligible for excluding any inter-modal interaction. For that reason the tails have to be short, the shortest value being obtained if the lateral refractive index contrast is just below the first order mode cut-off contrast. The corresponding maximal ridge heights are calculated for the various cover layers, using the 70-nm thick Si_3N_4 core layer (see Table 3).

Although maximal ridge heights lead to minimal channel mode evanescent field decay lengths, in view of technological tolerances in practice (slightly) lower ridge heights are chosen (see Table 3) to assure mono-modality. Furthermore, this allows for an easy fabrication scheme, as all ridge heights can be defined using only one channel mask. The corresponding evanescent field decay length values are also shown, allowing for a minimally required inter-channel distance of ~ 15 μm.

5.6. The splitting and combining functions

From the various types of 3-dB splitting and combining functions, such as 3-dB couplers, multimode interferometers and Y-junctions the latter type is chosen. The main reason for this choice is the simplicity; furthermore, a precise 1:1 splitting ratio is not required. The Y-junction has two functions: to split the power and to bring the powers on the desired channel distance. Because of the low lateral contrast, the splitting angle has to be small in order to prevent radiation losses at the splitting point. At the other side, a small angle requires long channels for obtaining the required channel distance, in that way increasing the propagation loss. Dependent on ridge height and channel losses, an optimum can be found. Having channel losses of 0.85 dB/cm and a ridge height of 0.7 nm, the optimum splitting is obtained by using two S-shaped bends with a bending radius of about 50 mm. The junction losses are calculated to be about 1.5 dB. In fact, a combiner is a reversed splitter, enabling the use of the same lay out.

5.7. The electro-optic phase modulator

Within each interferometer branch a phase modulator has to be inserted, both modulators being driven in counter-phase. ZnO will be used as electro-optical material, its characteristics allowing for AC modulation only. The driving voltage has to be low, preferentially at the 5-V level and has to be swept over a phase range π.

Table 3
Channel parameters using the 70 nm Si_3N_4 core layer and 4 μm channel width

	Water cover $n_c = 1.33$	SiO_2 cover $n_c = 1.46$	Gelatine cover $n_c \sim 1.5$	Polyimid cover $n_c \sim 1.6$	ZnO ($\sim$ 350 nm) –SiO_2 cover*, $n_{ZnO} = 2.0$
Critical ridge height (nm)	0.9	0.85	0.83	0.8	~ 6
Used ridge height (nm)	0.7	0.7	0.7	0.7	2.0
Evanescent field decay length at used ridge (μm)	~ 2	~ 2	~ 2	~ 2	~ 4

* This situation will be explained in more detail in Section 5.7.

Just as to the chemically induced phase change, the ZnO-based electro-optically induced phase change in each branch (see Fig. 14) can be written as:

$$\Delta\varphi_{e-o} = \frac{2\pi}{\lambda_0} L_{elec} \Delta N_{eff_{e-o}}, \tag{8a}$$

with L_{elec} is the electrode interaction length ($L_{elec} < L_{zno}$), and

$$\Delta N_{eff_{e-o}} = \frac{\partial N_{eff}}{\partial n_{ZnO}} \Delta n_{ZnO} + \frac{\partial N_{eff}}{\partial d_{ZnO}} \Delta d_{ZnO}. \tag{8b}$$

As the piezo-electrical effect of ZnO is very small [36], the most right-hand term in Eq. (8b) can be neglected. The coefficient $\partial N_{eff}/\partial n_{ZnO}$ is determined by the waveguide parameters used. For TE-light it can be derived [40]:

$$\Delta n_{ZnO} = 1/2 r_{13} n_{ZnO}^3 E_{ZnO}, \tag{8c}$$

with E_{ZnO} the field strength in the ZnO layer in the vertical direction, and r_{13} is the appropriate electro-optical coefficient, being 1.4×10^{-12} m/V [36].

Because Δn is linear to E_{ZnO}, the sign of the external electric field E_{ZnO} determines the sign of the induced phase change. The modulators have a configuration as is shown in Fig. 10, both having the Si wafer as a common bottom electrode. Applying driving voltages with reversed polarities to the two top electrodes therefore doubles the electro-optically induced $\Delta\varphi_{ZnO}$. Combining this with Eqs. (8a), (8b) and (8c) results in an MZI phase change:

$$\Delta\varphi_{e-o,MZI} = r_{13} n_{ZnO}^3 \frac{2\pi}{\lambda} L_{elec} \frac{\partial N_{eff}}{\partial n_{ZnO}} E_{ZnO}. \tag{8d}$$

Lowering $V_{2\pi}$ can therefore be obtained by:

- increasing the (electrode) interaction length L_{elec};
- decreasing the used wavelength;
- maximising $(\partial N_{eff}/\partial n_{ZnO})E_{ZnO}$.

In Fig. 11, the theoretical dependence of the required modulation voltage as a function of the ZnO layer thickness is given, using the modulator configuration shown in Fig. 10. The reason for the presence of the Si_3N_4 layer will be given in Section 6 item (8). The oxide layer thicknesses at a given ZnO layer thickness are taken in such a way that the total electrode-induced attenuation is equal to 0.01 dB for the used TE-polarised light at $\lambda =$ 632.8 nm. The driving voltage shown in Fig. 11 can be regarded as the voltage–length product (V cm), yielding V_π [41].

From Fig. 11 it follows that the driving voltage does not critically depend on the exact thickness of the ZnO layer. In view of the slow ZnO deposition process, a thickness of about 350 nm has therefore been selected. Although this slab guide is multi-modal, application of tapers in the ZnO layer as will be described in Section 5.9, will afford an adiabatic transfer of the incoming TE_0 mode to the modulator. The corresponding minimum values of the thicknesses of the substrate and cladding layer, required for the electrode-induced losses to be smaller then 0.01 dB/cm, are calculated to be about 500 nm. For safety reasons, we have chosen those layers to be 600 nm thick, resulting into a slightly enlarged theoretically calculated driving voltage–length product of 15 V cm.

The single-mode ridge height is defined also here in the Si_3N_4 layer. In this way, photolithographical patterning of the (very reactive) ZnO can be conveniently avoided.

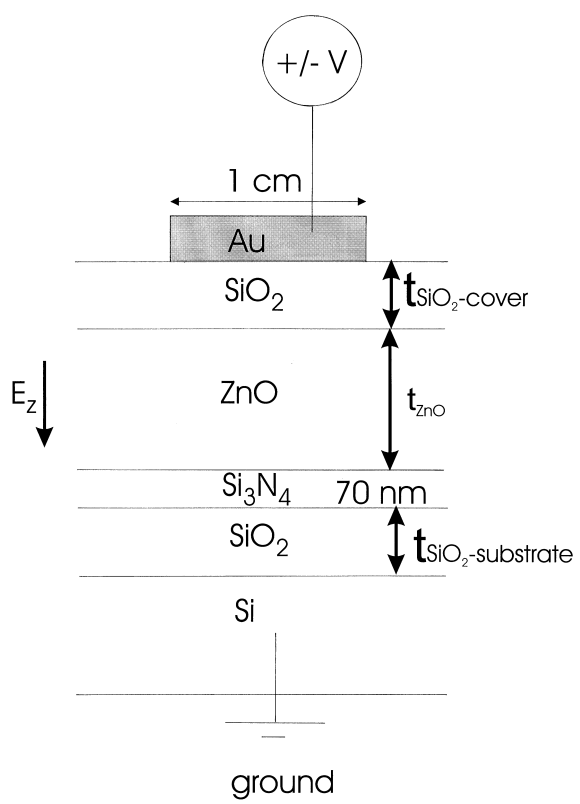

Fig. 10. Cross-section along the propagation direction of the modulator layer structure.

5.8. The fibre-to-chip interconnection unit

The main requirement for an efficient fibre-to-chip coupling is a good match of the field profiles of the single-mode fibre mode and the waveguide channel mode. To obtain a large overlap between the modal field of the fibre and the channel waveguide, either the fibre can be adapted to the channel waveguide (lensing and/or tapering the fibre) or vice versa. In view of the commercial availability of standard fibre cleavers and the desired compatibility with mass production, the latter option is more attractive. Using very thin (''loose-mode'') layers, a high coupling efficiency can be obtained. Here the loose-mode

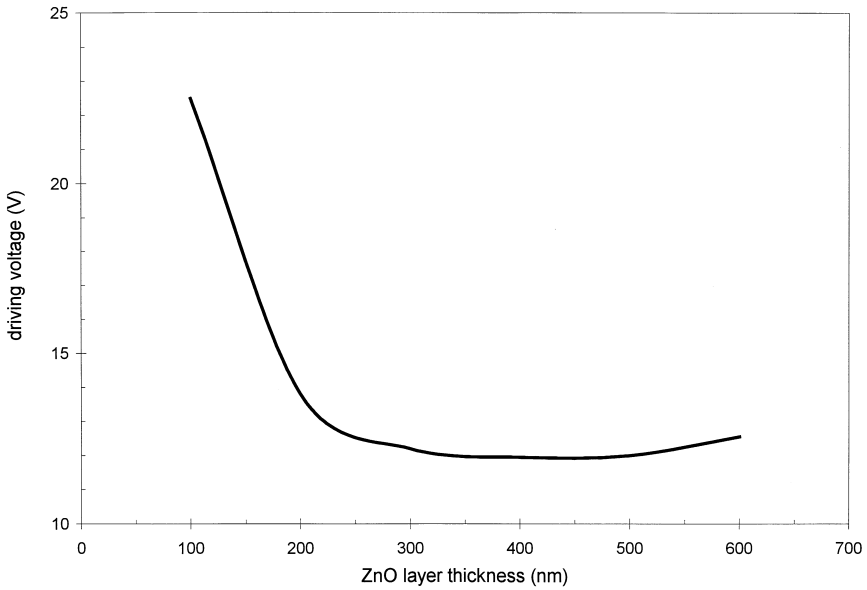

Fig. 11. Driving voltage as required for a 2π phase modulation as a function of the ZnO thickness. Here, the modulator geometry as shown in Fig. 10 is used, resulting into an extra electrodes-induced 0.01 dB/cm propagation loss (TE-polarised light at 633 nm, electrode interaction length $L_{elec} = 1$ cm).

structure should be adapted to match at the wavelength used, being 633 nm, to the mode of a fibre with a core of 4 μm and waist of 4.75 μm, which is typical for single-mode operation.

In Fig. 12a the loose-mode configuration yielding optimal results is depicted, as derived elsewhere [32]. The optimal channel width and ridge height are 4 μm and 2 nm, respectively: the corresponding TE_0 fibre-to-chip cou-

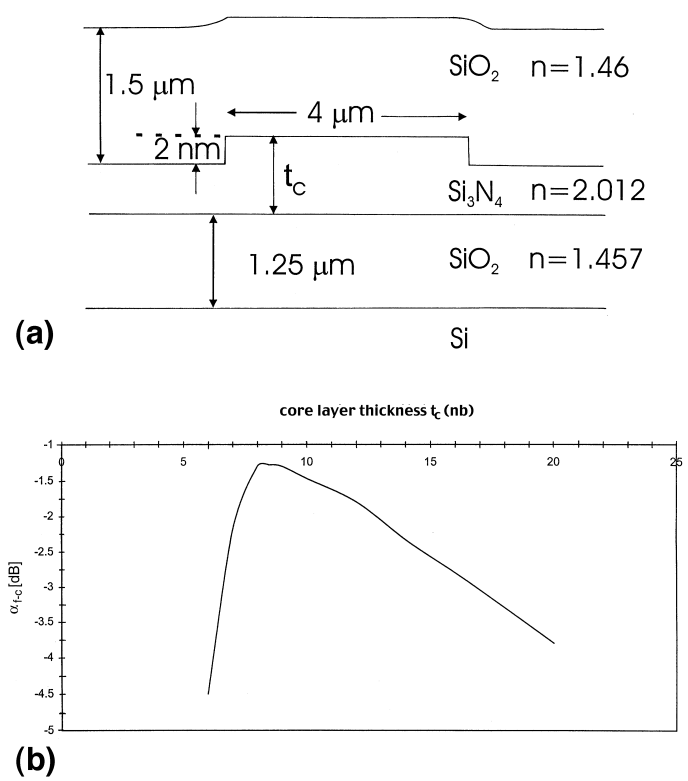

Fig. 12. Cross-section of the loose-mode waveguide configuration used for efficient fibre-to-chip coupling (a) and the corresponding fibre-to-chip coupling loss $\alpha_{\text{fibre-chip}}$ (for TE-polarised light at 633 nm) as function of the Si_3N_4 layer thickness (b).

pling loss α (in dB) as a function of the thickness of the nitride core layer is depicted in Fig. 12b, using TE-polarised light ($\lambda = 632.8$ nm).

According to this simulation and neglecting reflections, a coupling loss from fibre to the TE_0 mode as low as 1.4 dB ($\sim 75\%$ coupling efficiency) is therefore possible, provided the Si_3N_4 layer thickness is accurately controlled to a value of 8 nm. Although that can be done, in practice a safer value of ~ 15 nm is used, as a compromise between wafer yield and coupling efficiency. The corresponding TE_0 coupling efficiency is 3.0 dB, while the corresponding coupling loss for TM polarisation is ~ 5.0 dB (not shown).

The theoretical mode overlap values refer to a perfect alignment between the fibre and the channel waveguide. Regarding a 5% decrease as acceptable, the maximum allowable misalignment in the lateral, vertical and angular orientations are 2 μm, 1 μm and 0.5°, respectively [32]. In view of the typical single-mode fibre characteristics, showing an inaccuracy in the core positioning with respect to the centre of the fibre of $\sim 1\%$ (~ 1–2 μm), this is not trivial.

Using the well-known wet-etched V-shaped groove obtainable in silicon ⟨100⟩ wafers [42] (see Fig. 13) and using a double mask technique [43] for nearly perfect lateral alignment, these alignment requirements can be met. The remaining V-groove plane preventing close physical contact of the fibre facet end with the channel end facet is removed using a sawing procedure (see Section 6). Additional advantage is the adjustability of the fibre tip position along the vertical direction (see Fig. 13b), that direction being the most sensitive to misalignment.

The attenuation losses of the TE_0 and TM_0 mode in this loose-mode section are completely determined by the layer thickness of the substrate material SiO_2. With a thickness of ~ 1.25 μm, these values are ~ 20 and 100 dB/cm for the TE and TM polarisation, respectively. To obtain acceptable TE attenuation values the length of the loose-mode section should be as small as possible. In practice, a value of 100 μm is used, yielding the TE attenuation is ≤ 0.2 dB. The corresponding TM_0 mode attenuation is ~ 1 dB.

The same type of coupling unit can be applied for coupling the light to the output fibre. Because here the mode power is the only parameter of interest, the single-mode fibre can now be replaced by a multi-mode fibre increasing the coupling efficiency even more.

5.9. Discussion

The optimisation of the individual components delivers multi-layer cross-sections being strongly dependent upon the desired function, as shown in Table 4.

One approach to cope with that problem is to look for the best compromise [18]. Holding the thickness of all SiON layers constant over the whole chip will result into a

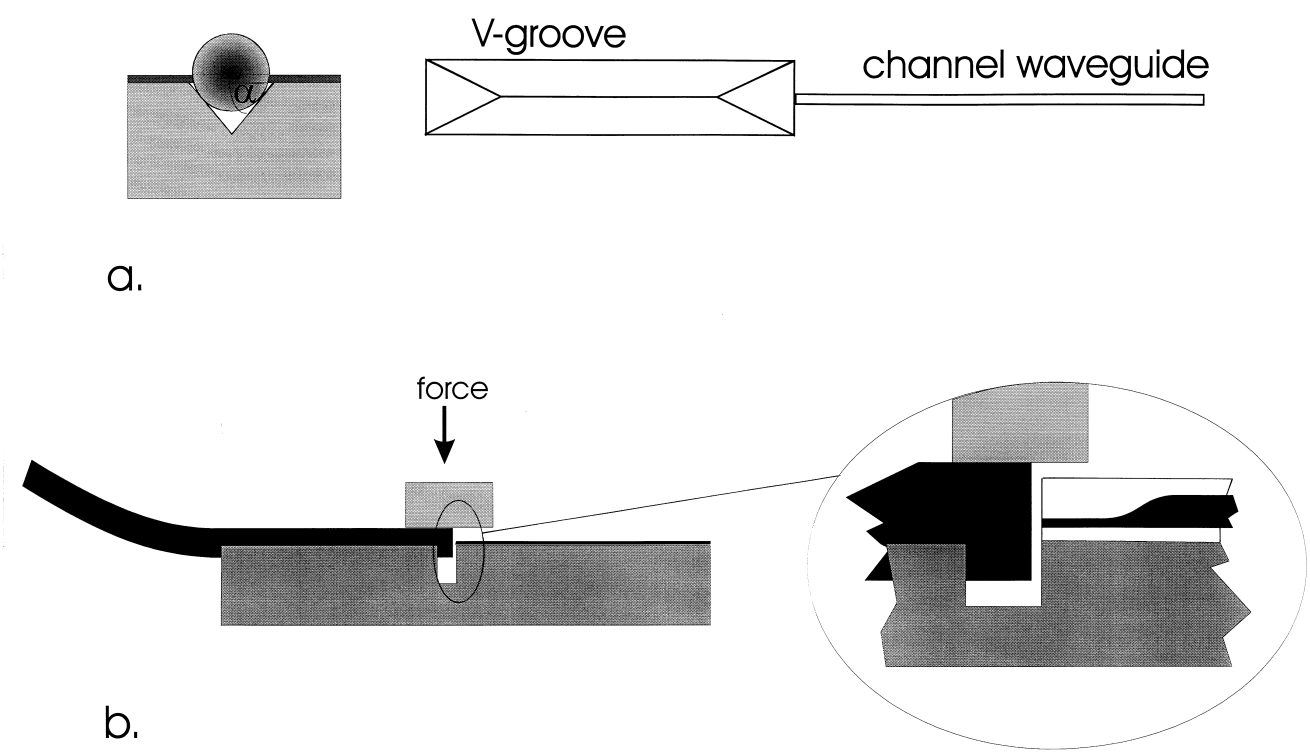

Fig. 13. Schematic representation of the fibre-to-chip connection unit. Cross-section of the silicon V-groove (left) and top-view of this groove and the aligned channel waveguide (right), see (a). Side-view cross-section of the adjustable fibre-to-chip interconnect, see (b).

Table 4
Layer thickness values for the different functions

	$t_{substrate,SiO_2}$ (nm)	t_{core,Si_3N_4} (nm)	$t_{cladding,SiO_2}$ (nm)	t_{ZnO} (nm)
TE/TM polariser	1250	70	1500	0
Modulator	600	0	600	350
Sensor window	> 1250	70	0	0
Fibre–chip coupler	> 8000	15	> 8000	0

remarkably worse performance. Taking the thickness of the core, the cladding and the substrate layers at values of 70, 1500 and 1250 nm, respectively, should result into a modulation voltage of 56 V instead of 15 V and a fibre–chip coupling efficiency of 8% instead of 75%.

Our policy however will be to maintain the optimised structures for the individual components by local deposition or local etching and connect these different structures by applying transversal tapers. These tapers form the transition regions for matching two waveguides with different cross-sections to each other [44]. The taper-induced loss is determined mainly by the taper angle. Properly designed tapers add no extra loss: the required taper angle for these so-called *adiabatic* tapers is generally small [45]. The FDBPM method enables calculation of the taper losses both for simulation and for verifying purposes. Experimentally, a tapered ZnO segment can be obtained by sputtering using a shadow mask, while tapering of the SiON layers can be achieved by wet etching (see also Section 6).

The final layer structure aimed at is presented in Fig. 14. The Si_3N_4 core layer has everywhere the same thickness of 70 nm, except in the fibre–chip coupling region (having a length of 100 μm only). Here, it will be gradually tapered down to a thickness of 15 nm. To have

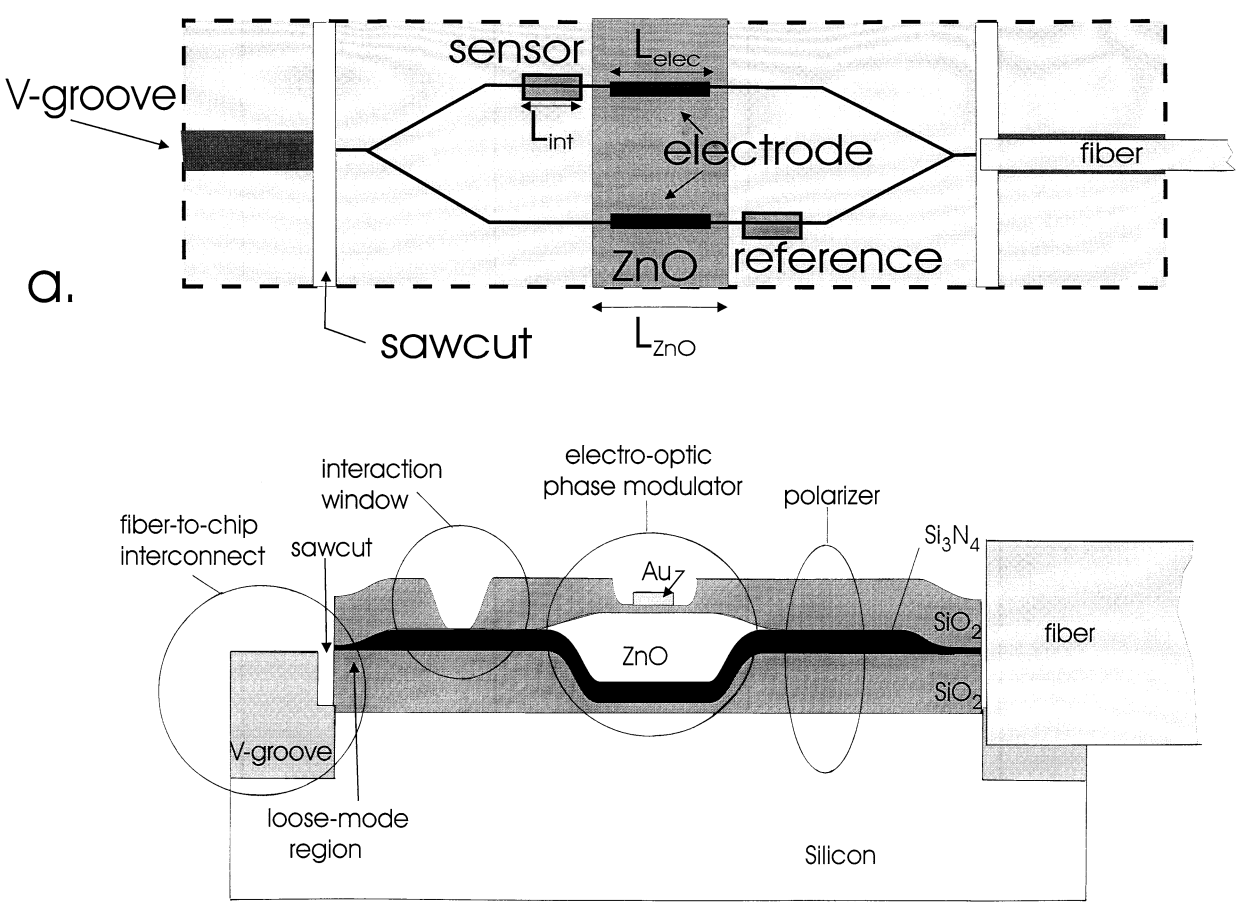

Fig. 14. Schematic top-view (a) and side-view cross-section (b) of the IO MZI. For convenience, only the outcoupling fibre is shown.

functional tapering losses smaller than 0.1 dB the (linear) taper angle θ should be smaller than 0.03°. The ridge type waveguiding channels are defined in the Si_3N_4 layer and have a ridge height of 2.0 nm both in the fibre-to-chip coupling unit and the modulator section, and 0.7 nm elsewhere.

The ZnO layer will be applied in the modulator region only and will be tapered by using a shadow mask. The absence of ZnO outside the modulator region has several advantages. Firstly, the definition of the interaction windows has not to be achieved on top of the fragile crystalline structure of ZnO, which is known to show only low resistance to almost every liquid [37], but on the very stable Si_3N_4 layer. Secondly, the overall optical throughput of the MZI will increase, as the intrinsic waveguide loss of ZnO, although relatively low, is still larger than that of Si_3N_4 (typically 1 and ≤ 0.2 dB/cm for slab guide attenuation at a wavelength of 632.8 nm, respectively). The ZnO taper angle should be smaller than $\sim 1°$ to obtain functional tapering losses smaller than 0.1 dB.

In this modulator region the stack Si_3N_4–ZnO acts as waveguiding core, both isolating SiO_2 layers preventing electrode (silicon and gold)-induced attenuation, can be significantly reduced in thickness without a relevant increase of the propagation losses. The SiO_2 substrate layer will show a thickness of 1.25 μm except at the modulator region. Here, the thickness is reduced to 600 nm. Although this thickness reduction does not act as a waveguide taper, the corresponding angle is also restricted to limited values, as it actually acts as a curve for the waveguide on top. To prevent curvature-induced scattering, a taper angle smaller than $\sim 10°$ [38] is required. The SiO_2 cladding layer shall have a thickness of 1.50 μm except in and near the modulator and the sensing function, where it will be 600 and 0 nm, respectively. The required tapering angle of the sensing window depends on the refractive index distribution within the window; for convenience, we will apply the value of 10°. The taper angles at the modulator region are not relevant however because the evanescent field does not penetrate so far.

Using these values, the corresponding losses for the all important optical components are calculated (see Table 5). For convenience, the losses in the sensing window are given using several different ''sensing layers''.

From these numbers it is clear that the sensing window should be filled, as an air-clad waveguide shows significant losses. In view of the lengths of the different components (see below), these values result in a theoretical overall TE/TM polarisation ≥ 30 dB.

Large interaction lengths of the sensing unit and the modulator should increase the sensing effect and decrease the required modulation voltage, respectively, but should need an extended chip area. We have chosen them to be 4 and 8 mm, respectively.

5.10. Electronics

The electronic system has two main functions:

- generation of the driving voltage with adjustable amplitude;
- demodulation of the signal.

Furthermore, the system should be flexible, allowing the implementation of feedback loops (for example, maintaining the modulation voltage to exactly $V_{2\pi}$), be easy to use, allow for stand-alone and computer-controlled use, etc. For reasons of compatibility with future developments, a standardised approach has been used [46]. In Fig. 15 a functional scheme of the designed electronics is depicted, which will be discussed briefly.

The ''controller'' block provides for the main functions and the communication with the sub-controllers (the stimulus and the response blocks), performs the calculations on the raw MZI signals and sends the results to the display. The system can be run stand alone, but because it is also made (field)programmable, it is able to perform additional functions. This makes the system very flexible and easy to use. It is also possible to connect the system directly to a host computer. This enables advanced measurements over extended periods where data storage is needed. Optionally, the system can receive extra instructions from a separate keyboard.

The ''stimulus'' block generates the triangular driving voltage(s) to be applied to the two modulator electrodes. The effective amplitude is regulated to a value of $V_{2\pi}$, using the feedback loop as discussed in Section 3.

The ''response'' block converts the modulated optical signal into a TTL-levelled electrical signal and generates raw ''phase data'' for the ''controller''. It consists of a photodiode, an amplification circuit, an RC network per-

Table 5
Attenuation values of the (quasi)TE/TM 0-th order modes for the different components

	Fibre-to-chip coupling loss (dB)	Loose-mode waveguide* (dB)	Basic 70-nm channel guide (dB/cm)	Phase modulator region (dB/cm)	Sensing window with n_c 1.0 (dB/cm)	1.33	1.50
(quasi)TM_0	~5.0	~1	~8	0.2	~3000	~450	~1.1
(quasi)TE_0	~3.0	0.2	0.018	0.01	3.7	0.15	0.008

* This waveguide section has a length of only 100 μm.

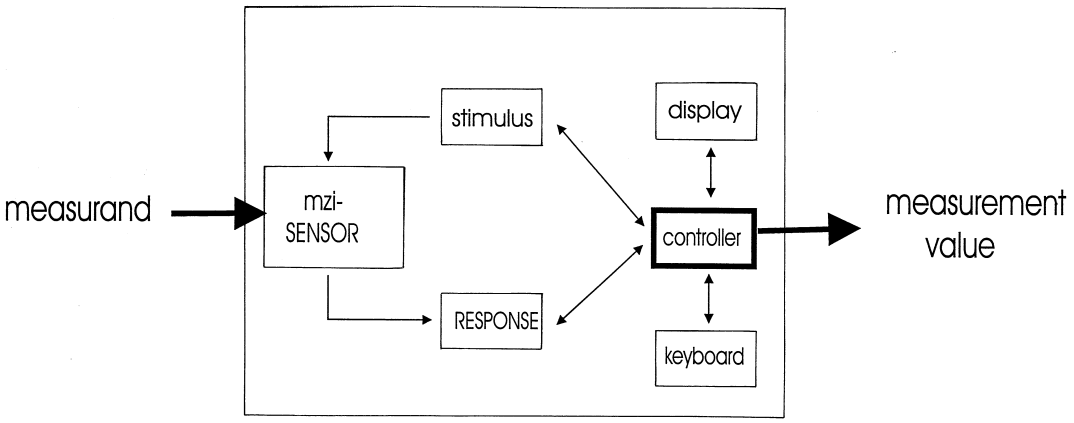

Fig. 15. Functional scheme of the electronic system. See the text for explanation.

forming the AC coupling, a zero-level comparator and a micro-controller measuring the time T (see Fig. 5).

The phase resolution is principally limited by the accuracy of the time interval measurement. Hence, the phase resolution which can be obtained using this (de)modulation technique is depending on both the clock rate and the frequency of the triangular modulation voltage. The latter is determined by the desired application, as the applied frequency should exceed the maximum frequency going with the parameter to be detected. In theory, for every specific application an optimal choice can be made. However, in this prototype electronic system, a compromise between phase resolution and applicability in real sensor systems has been made. The chosen drive frequency of 56 Hz restricts the maximum detectable frequency related to the parameter to be detected to ~ 10 Hz, and allows a phase resolution of $\sim 5 \times 10^{-5} \times 2\pi$. We want to stress that the latter value is by no means the limit of the sensor concept.

6. Fabrication

The masks contain both stand alone individual components and complete MZI systems. The latter are located in

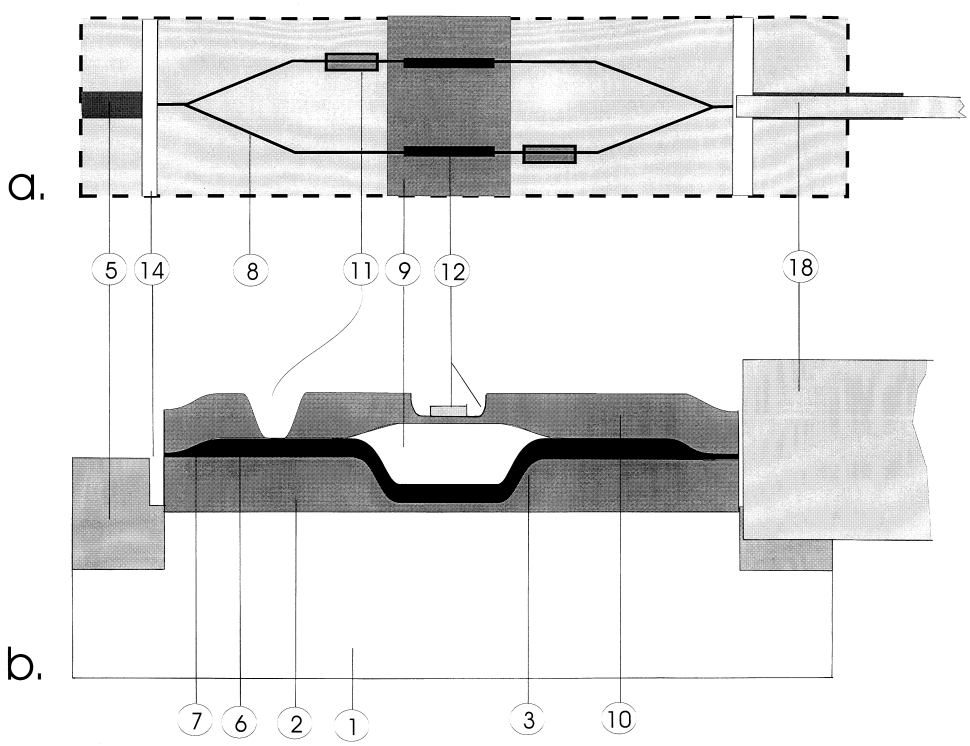

Fig. 16. Top-view (a) and side-view cross-section (b) of the IO MZI, showing the numbers of the main fabrication steps in relation to a specific function.

groups of five, the lateral dimensions of such a unit corresponding to 55×3 mm. This chip area is used as a standard for packaging. In the following, the most important wafer processing steps, as elucidated in Fig. 16, will be briefly described.

(1) Starting point of the optical chip is a highly conducting (0.010–0.018 Ω cm) 3-in. silicon ⟨100⟩ wafer.

(2) Thermal wafer oxidation (at 1150°C), resulting into a 1500-nm thick SiO_2 layer at both sides of the wafer.

(3) Determination of the Si crystal planes orientation with an accuracy better than 0.1°, this being relevant for proper orientation of the mask in order to be able to make well-shaped V-grooves.

(4) Local etching of the SiO_2 layer in the modulator region using $HF:NH_4F \equiv 1:7$ solution (BHF), for reducing the SiO_2 layer thickness to 750 nm.

(5) Etching of V-grooves with a KOH solution (73–74°C): V-groove width 145 μm. During this process step also the SiO_2 layer is partly etched off, diminishing its thickness to 500 nm in the modulator region and to 1250 nm elsewhere.

(6) Deposition of 70 nm Si_3N_4 using LPCVD at 800°C.

(7) Etching the loose-mode regions using BHF. The resulting layer thickness is adjusted to a value of 15 nm.

(8) Channel ridge definition using BHF. By applying the two-step photolithography method [43] a ridge height of 2.0 nm is etched in the loose-mode regions and the phase modulator region, and 0.7 nm elsewhere.

(9) Growing of the ZnO layer with a thickness of 350 nm using RF diode sputtering at 200°C [33]. Using a shadow mask, this deposition is restricted to the modulator region. The geometry of the mask is adjusted to the required tapering angle (see for that Section 7.7).

(10) Growing of the 1.5-μm thick SiO_2 layer using PECVD at 300°C.

(11) Etching of the sensing windows (length 4 mm, width 50 μm) using BHF.

(12) Fabrication of the top electrodes using the lift-off technique. First the SiO_2 layer thickness at the electrode positions is reduced to a thickness of 500 nm using reactive ion etching (RIE), directly followed by metal deposition (a ~5-nm Cr adhesion layer and a 300-nm Au layer) using electron beam sputtering. By applying a lift-off process the excess metal is removed. In Fig. 17, a SEM photograph of the layer structure at this location is shown.

(13) If desired by the specific application, the appropriate sensitive layer is applied.

(14) Removal of the remaining Si V-groove plane preventing close physical contact (see Fig. 13) using a diamond saw with a blade width of 40 μm. The corresponding saw cut depth is ~100 μm.

(15) Dicing of the individual sensor chips.

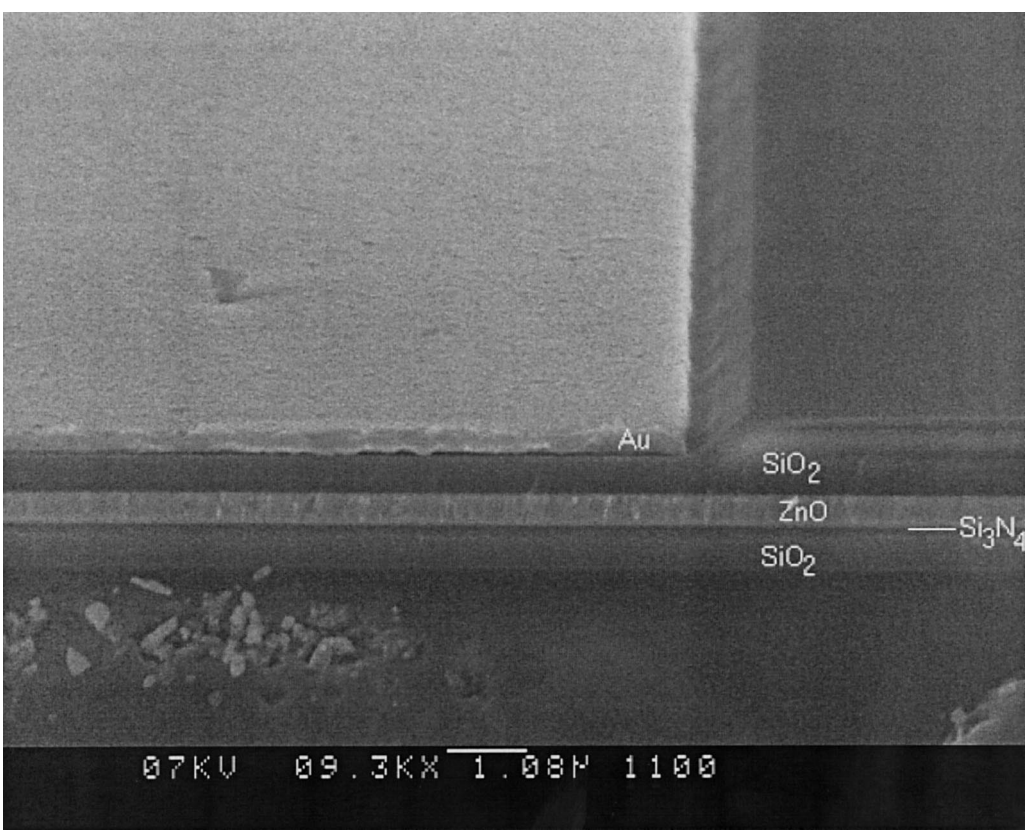

Fig. 17. SEM picture of the cross-section along the propagation of the electrode structure, as deposited in an etched region of the covering SiO_2 layer. The ZnO layer thickness is ~350 nm, while the remaining SiO_2 layer thickness is ~550 nm (preventing electrode-induced optical losses). The SiO_2 boundary shows an angle of ~45°, resulting from an RIE process.

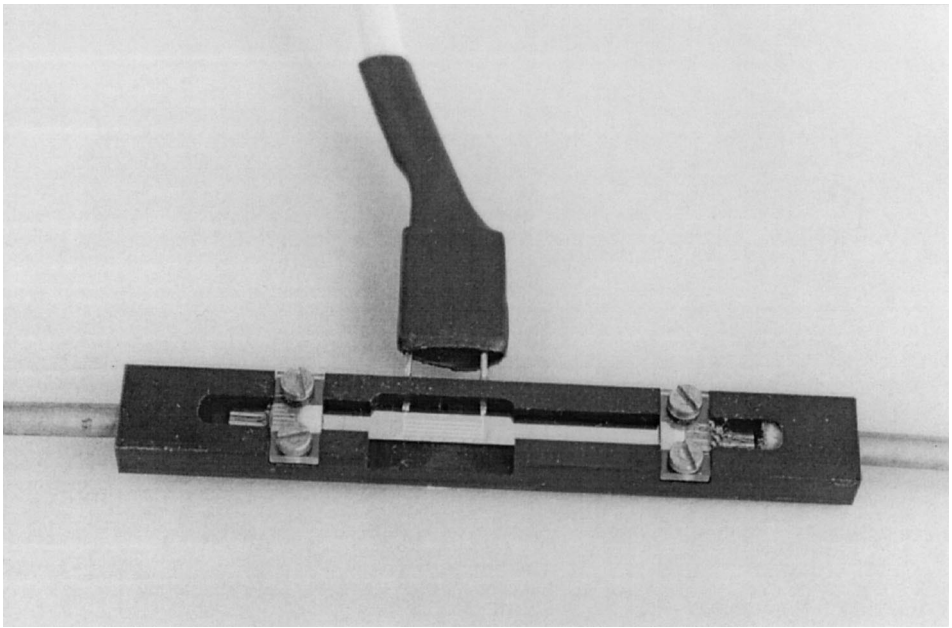

Fig. 18. Photograph of the packaged optical chip, clearly showing the electrodes and the fibre-to-chip connection units. The chip contains four MZI structures, which can be individually exited using the appropriate V-grooves. The four electrode pairs, fabricated in parallel, are connected through wire bonds to the same driving electronics.

(16) Mounting of the chip in plastic (PVC) package (see Fig. 18).

(17) Wire bonding of the top electrodes.

(18) Connecting the in- and out-coupling fibres to the fibre-to-chip connection unit.

In the last step, either index matching gel ($n = 1.50$) or a transparent, UV curable glue ($n = 1.50$) is used (Permacol, type 27/3). The glue shows a very slight shrinkage during curing. In case of the glue, the position of the fibre is fixed after optimising the coupling efficiencies. The parameters of the single-mode input fibre are: outer fibre diameter 125 mm, core diameter 4 μm, NA = 0.11 ± 0.01. The parameters of the multimode output fibre are: outer fibre diameter 125 μm, core diameter 50 mm, NA = 0.20 ± 0.02. In Fig. 18, a photograph of the packaged device is shown.

The packaged optical chip is now connected to the He–Ne laser and the external electronics.

7. Testing results and discussion

In this section results of testing both the individual components and the complete sensing system will be presented. Individual components will be treated in the following sequence: straight channel waveguide, Y-junction, TE/TM polariser, fibre-to-chip coupling function, modulator, sensing unit and tapers. The section ends with a discussion of the phase resolution and long-term stability as obtained with the complete system. An application example is given.

7.1. Straight waveguide channels

Using the cut-back method, the propagation losses of the transport channels at a wavelength of 632.8 nm have been determined, being 0.85 ± 0.15 dB/cm.

The exact value of the N_{eff} of this channels, being relevant only for obtaining the sensitivity, cannot be determined directly. In fact for that dummy channels are needed, being located close to the MZI on the same chip. They have to be provided with grating couplers with a well-defined period for coupling the light out of the waveguide. From the coupling angle the N_{eff}-value can be determined. It is simpler however to extend the calibration of the complete system, yielding not only the determination of $\Delta\varphi_0$, but also the waveguide sensitivity itself.

7.2. The splitting and combining functions

Splitting ratios always deviate a little from the desired 1:1 value. Experimentally, the typical splitting ratio is found to be 0.48 ± 0.02: 0.52 ± 0.02. The typical losses of the Y-junctions are measured to be ~ 1.5 dB/junction.

7.3. TE / TM polariser

The TM/TE rejection ratio of both a straight waveguide and the complete MZI (the MZI has been brought into the state of constructive interference by applying an appropriate voltage on one of the modulators) has been

Table 6
Typical fibre-to-chip coupler characteristics, with channel width of 4 μm

Si_3N_4 layer thickness (nm)	Channel ridge height (nm)	Calculated modal overlap (%)	Measured coupling efficiency (%)
15 ± 2	2.0 ± 0.2	55 ± 5	50 ± 10

experimentally determined, the values being ~ 7.5 dB/cm and ≥ 30 dB, respectively. These values agree well with the ones, theoretically calculated in Section 5.3, being 8 dB/cm and 33 dB, respectively.

7.4. The fibre-to-chip interconnecting unit

Elsewhere [32], we have published an extensive report on this component. Here we will limit ourselves to presenting the results as obtained from a large number of 4-μm wide channel waveguides from various batches (see Table 6).

From Table 6 it can be concluded that the experimental and theoretically obtained values of the coupling efficiency agree well with each other.

7.5. The electro-optic modulator

The electro-optical phase modulation experiments are performed using an optical chip without interaction sensing windows. A typical response, using the voltage feedback loop (see Section 3.2.1) is shown in Fig. 19. In Fig. 19 amongst others the triangular driving signal, as applied to one of the electrodes is plotted as a function of time, just as the resulting optical signs, the synchronisation signal as used for the demodulation, and the comparator output signal.

An effective driving signal with a top-to-top value of 43 V (21.5 $V_{top-top}$ with reversed polarity to both electrodes) to both appears to result into a phase modulation of exactly 2π, as is visible in Fig. 19. In view of the electrode length of 8 mm, this is equivalent to a voltage–length product V_π of 17 V cm, which is found to be typical for the chips measured. This value is in good agreement with the theoretical one, i.e., 15 V cm (see Section 5.7). Note that the required amplitudes of the triangular driving voltage as applied to the electrodes are ~ 11 V only. The modulation depth is typically 13 dB, corresponding to a value of the visibility factor V equal to 0.90.

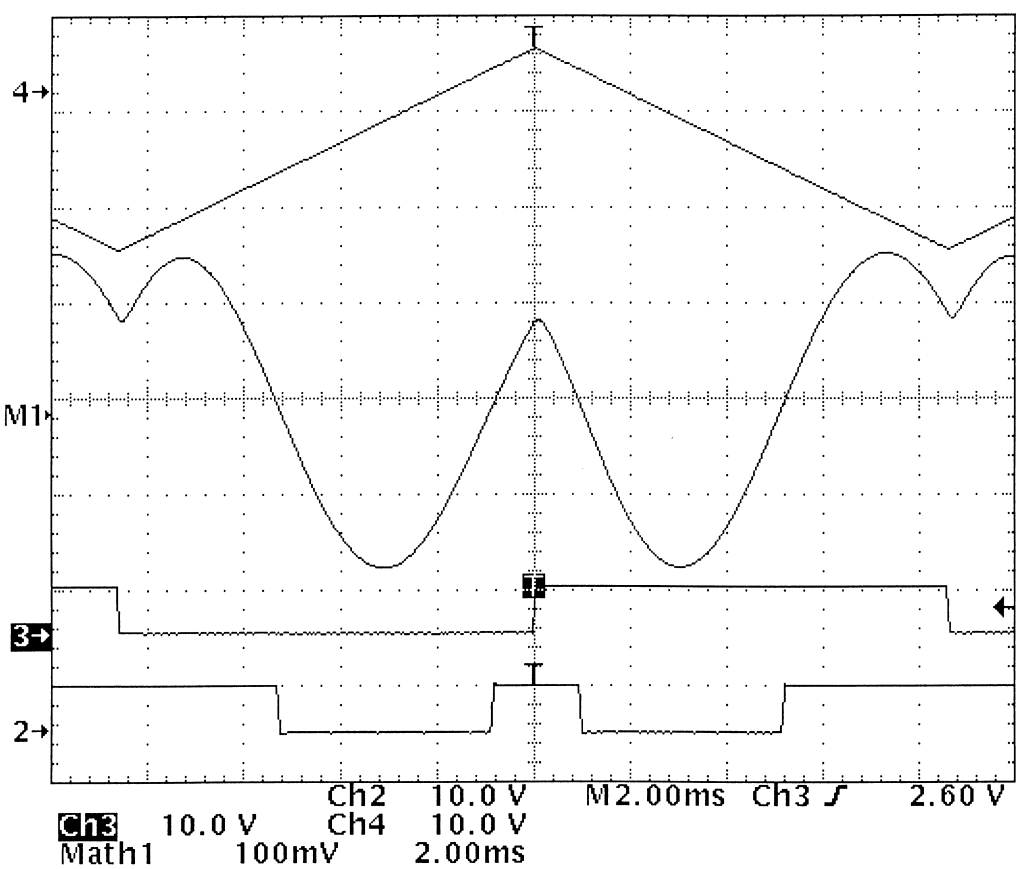

Fig. 19. Oscilloscope plot while using the device electronics in the $V_{2\pi}$ feedback loop with a triangular signal of 56 Hz, showing four signals from top to bottom: – the triangular driving signal as applied to each electrode of 8 mm length (21.5 $V_{top-top}$); – the resulting optical output after removing the DC bias by an RC network; – the synchronisation signal; – the comparator signal.

7.6. The sensing function

Experimental verification of the theoretically calculated sensitivity requires a very accurately known refractive index change of the sensitive material. For that we have chosen a liquid of which the composition gradually changes as can be realised by using a fluid injection system. The chosen fluids are ethanol $(n = 1.3602 \pm 0.0005)$ and methanol $(n = 1.3288 \pm 0.0005)$ at 20°C, as measured with an Abbe refractometer at 632.8 nm. For this homogeneous sensing the phase shift can be expressed as (see Eq. (2)):

$$\Delta\varphi_m = \frac{2\pi}{\lambda_0} L_{int} \Delta N_{eff} = \frac{2\pi}{\lambda_0} L_{int} \left(\frac{\partial N_{eff}}{\partial n_{liquid}} \right) \Delta n_{liquid}. \quad (9a)$$

For the given waveguide structure $\partial N_{eff}/\partial n_{liquid}$ is calculated to be $(20.0 \pm 0.5) \times 10^{-2}$ (see Section 5.4). With an interaction length of 4 mm and $\Delta n_c = (3.14 \pm 0.10) \times 10^{-2}$, the phase shift at 632.8 nm can be calculated to be:

$$\Delta\varphi(39.7 \pm 2.3)2\pi. \quad (9b)$$

Experimentally (without the modulation) it is found:

$$|\Delta\varphi_{methanol \rightarrow ethanol}| = 37.75 \times 2\pi; \quad (9c)$$

$$|\Delta\varphi_{ethanol \rightarrow methanol}| = 37.70 \times 2\pi. \quad (9d)$$

This match between theory and experiment is sufficient to show the validity of the theoretical calculation of the sensitivity. Nevertheless, the accuracies of the refractive indices of both liquids, as measured by the Abbe refractometer, are too low for an appropriate calibration of $\partial N_{eff}/\partial n_{sm}$. Hence, for accurate measurements, calibration using well-known concentrations of the measurand is required.

7.7. The tapering sections

To characterise the tapers, their geometry and their functional losses are relevant. Geometrical data can be obtained from SEM pictures and/or a profile scanner; the functional losses can be determined by subtracting the losses of straight channel guides from those containing the tapers.

The Si_3N_4 taper has to connect a 70- to a 15-nm thick layer. Using standard photo lithography a geometrical taper angle of only $\cong 0.25°$ could be obtained, corresponding with a taper length of ~ 12 μm. In terms of mode size however, the taper angle is quite large, because it converts the (transversal) mode waist from 4.75 to ~ 0.25 μm, corresponding to a mode size taper angle of $\sim 20°$; using FDBPM a taper loss of ~ 1.5 dB can be calculated. The latter value is experimentally verified to be $\sim 1.25 \pm 0.25$ dB.

Using special photolithography [45], the obtained taper angle appeared to be reduced to a value of $\cong 0.10°$, resulting in measured taper-induced loss ≤ 0.5 dB. As this value is regarded as sufficiently low, no further effort has been put in optimising this taper.

The ZnO linear taper angle is defined by the dimensions of the geometrical shadow mask and the spacer used [44]. Two mask geometries, as given in Fig. 20, are used. The resulting tapers show taper angles of 0.05° and 0.01°, respectively, as shown by using a profile scanner. Both tapers lead to negligible losses, as can be theoretically calculated and is experimentally verified. In practice, mask geometry I is used, as it enables a significantly shorter taper length.

The wet-etched SiO_2 tapers (see Fig. 21) show tapering angles of about 15°. The effects of the SiO_2 substrate layer taper on the losses of the modulator appear to be about 0.25 dB/taper. The excess compared to the calculated value (0.05 dB) can be ascribed to a irregularity of the taper near the thicker end (see Fig. 21a). If the sensing window is filled with water, both the calculated and the experimental functional taper losses are close to 0.1 dB/taper, being well-acceptable.

7.8. Device performance

7.8.1. Losses

The insertion loss of the complete device in case of completely constructive interference can be calculated from the losses of the individual components. In Table 7 this is summarised.

The sum of the losses of the individual components is ~ 16 dB. The experimentally obtained value is slightly larger, being ~ 20 dB. In view of the large amount of components on the chip, this increase with regard to the calculated sum of the losses of the individual components is not striking.

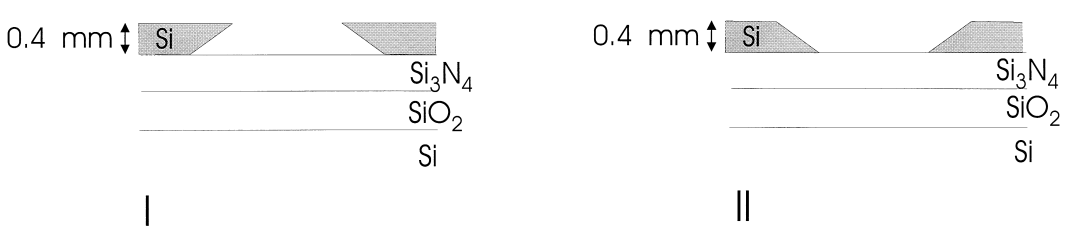

Fig. 20. The tested shadow mask geometries, in fact being KOH-etched Si wafers (I and II).

We also performed experiments on devices designed and realised for an MZI working at a 850-nm wavelength for use of a VCSEL (vertical cavity surface emitting laser) as a light source. These sensor systems show remarkably lower insertion losses, being only ~ 10 dB!

7.8.2. Device short-term phase resolution

To have a device short-term phase resolution $\Delta\varphi_r = 5 \times 10^{-5} \times 2\pi$, several conditions have to be fulfilled. Firstly, the sum of the uncertainties arising from laser, detector and electronic noise have to be smaller than $\Delta\varphi_r$. For the detector noise we derive:

$$1/2\, P_{source} \times -16\,\text{dB} > 10^5 \times \text{NEP} \times (\Delta f_{det})^{1/2}. \quad (10)$$

Here P_{source} means the power emitted from a pigtailed He–Ne laser; Δf_{det} is the band width of the detector; -16 dB represents the insertion loss at $\Delta\varphi_b = n2\pi$, and the factor $1/2$ arises from measuring at the quadrature point. In our experiments $P_{source} = 1$ mW, NEP $= 3.3 \times 10^{-14}$ W Hz$^{-1/2}$ and $\Delta f_{det} = 1000$ Hz, the modulation frequency being 56 Hz. Hence, the condition is amply obeyed, even in case of the experimentally obtained -20 dB insertion loss. The laser noise arising from a He–Ne gas laser is $\leq 1 \times 10^{-7} \times 2\pi$ [23].

Very essential is that the S/N ratio at the input of the comparator allows for a hysteresis setting around the zero crossing detection obeying the resolution requirement. Here also the noise generated by the electronics plays a part. As a detailed discussion goes beyond the scope of this contribution, we only state the experimental result: the noise originating from the electronics (including the comparator) to the system does allow for the required short-term phase resolution $\Delta\varphi_r = 5 \times 10^{-5} \times 2\pi$, provided that the amount of optical power on the detector exceeds ~ 5 nW. In the described practical situations, this requirement is easily fulfilled.

For experimental determination of the resolution, pigtailed optical chips have been connected to the driving and demodulation electronics. The driving modulation voltage is adjusted to $V_{2\pi}$, using the discussed feedback loop.

In order to exclude influences of fluctuations of the measurand, the sensing windows in both branches are filled with the sensing material, in our case a gelatine layer with a thickness of 2 μm. The refractive index of the gelatine, being sensitive to relative humidity (%.RH) is ~ 1.5, showing — at room temperature — a refractive index change of ~ 0.10 in the RH range 0–100%. Using a gelatine layer thickness of 2 μm, we are dealing with homogeneous sensing as the evanescent field is completely confined to the gelatine layer.

Experimentally, a short-term phase resolution of $\cong 1 \times 10^{-4} \times 2\pi$ is observed. This remarkably low value shows

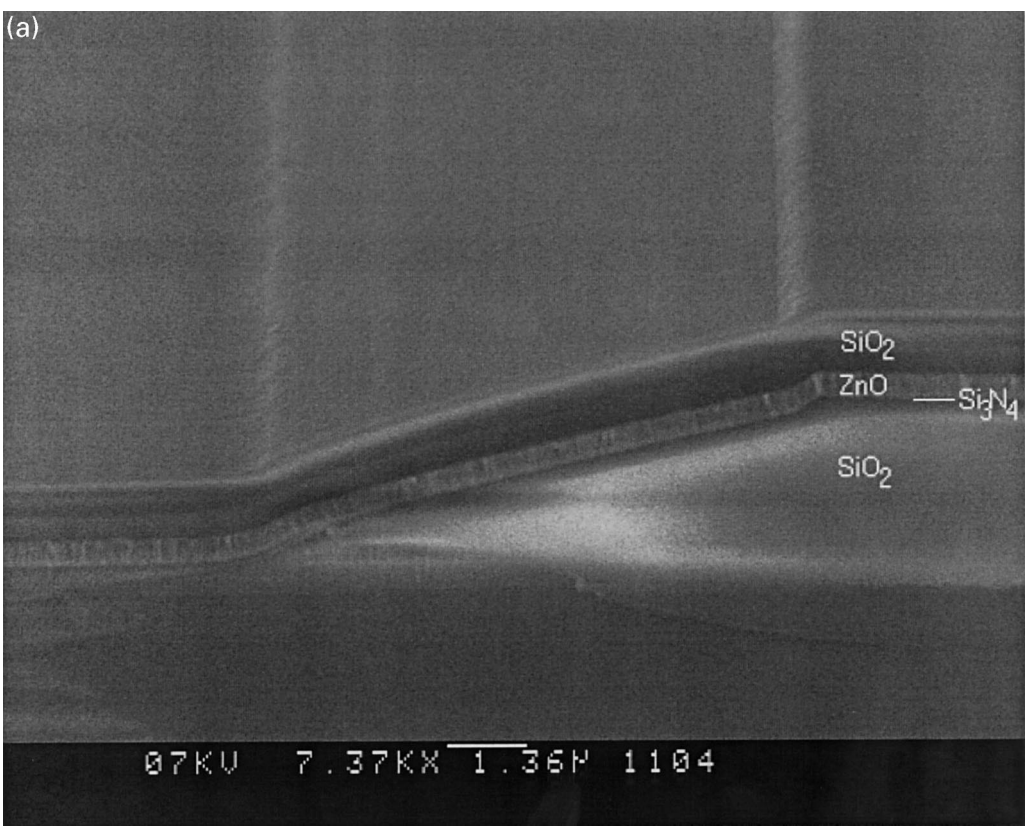

Fig. 21. Examples of SEM photographs of the tapered region in the SiO_2 substrate layer (a) and the cover layer (b), the latter for the interaction windows. In (a) also a (non-optimised) waveguiding layer stack in the modulator region is visible. For both SiO_2 tapers, the taper angle is $\sim 15°$.

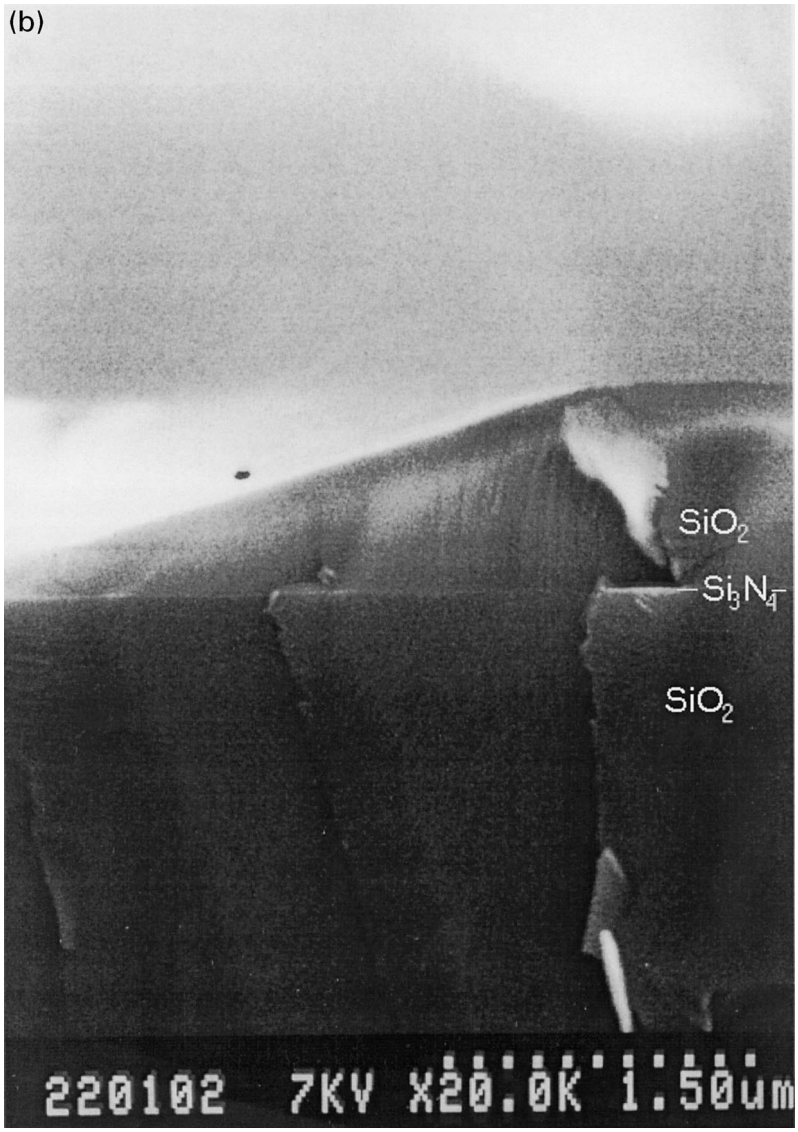

Fig. 21 (continued).

that the noise, corresponding to the optical circuitry is indeed always smaller than $1 \times 10^{-4} \times 2\pi$, as required. Furthermore, it shows that also the noise generated by the (electro)optical circuitry is very low. Because the electronics has not been optimised completely, an even better phase resolution should be possible.

7.8.3. Long-term stability

The long-term stability of this pigtailed IO MZI is probably even more important than the short-term phase resolution. This long-term stability, amongst others, expresses the influence of disturbing environmental effects (e.g., temperature variations) on the MZI response. For

Table 7
Summary of experimentally obtained loss contributions

Channel losses	Y-junctions	Tapers	Fibre–chip couplers
3 cm Si_3N_4: 0.85 dB/cm	2 Y-junctions: ~ 1.5 dB/junction	2 Si_3N_4 tapers: 0.5 dB/taper	sm* input: 3 dB
1 cm ZnO: ~ 3 dB/cm		2 ZnO tapers: ≤ 0.1 dB/taper	mm** output: 1.5 dB
		2 SiO_2 substrate tapers: 0.25 dB/taper	
		2 SiO_2 cover tapers: ≤ 0.1 dB/taper	
Total: ~ 6 dB	Total: ~ 3 dB	Total: ~ 2 dB	Total: ~ 4.5 dB

* sm: single-mode input fibre.
** mm: multi-mode output fibre.

these experiments two types of devices are used. In the first type both sensing windows are completely filled with gelatine. In the second type, the sensing windows are completely absent. Temperature differences between both branches are manifesting themselves in the performance of the first type (due to the temperature dependence of the association constant of the gelatine) but this effect does not hold in the second type.

The devices are placed in a non-thermostated room (showing a temperature change of several degrees over a day) and monitored continuously. Both (maximal) phase variations per hour and phase variations over a day are subtracted from these experiments. Maximal phase variations of $\sim 3\times10^{-4}\times2\pi$/h and $\sim 1\times10^{-4}\times2\pi$/h are found for the type one and type two devices, respectively. Phase values after a day (''drift'') deviate less than $30\times10^{-4}\times2\pi$ and $20\times10^{-4}\times2\pi$ from the starting value for both types, respectively. The latter means an averaged long-term stability (''drift'') of are $\sim 1\text{–}2\times10^{-4}\times2\pi$/h and $\leq 1\times10^{-4}\times2\pi$/h, respectively. Comparing with previously reported MZI related values [4,5,13–19] these remarkably good value is found in the nearly completely balanced geometry, the smaller temperature gradients due to the high thermal conductivity of the Si substrate and the

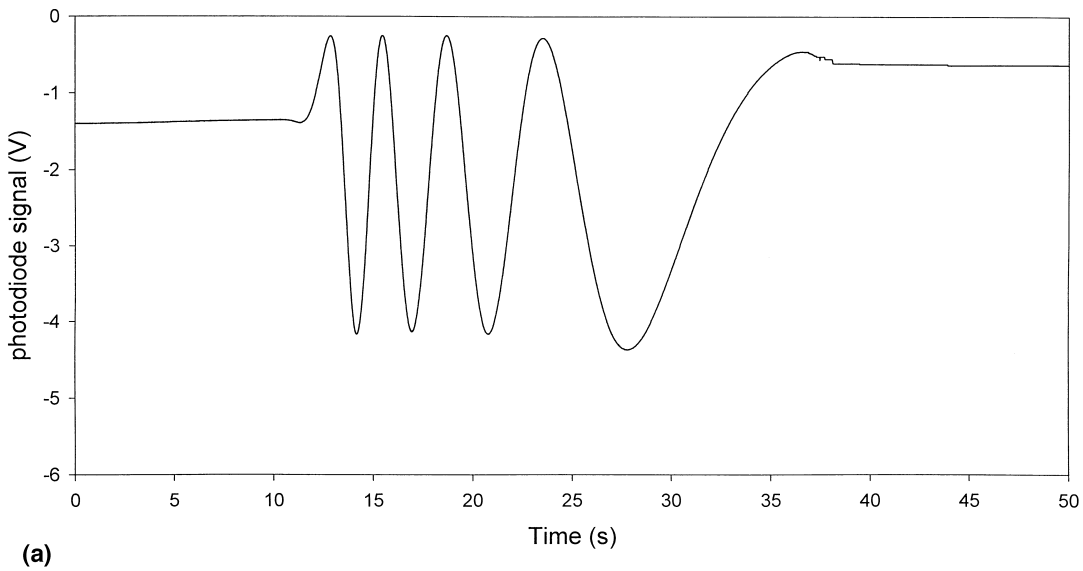

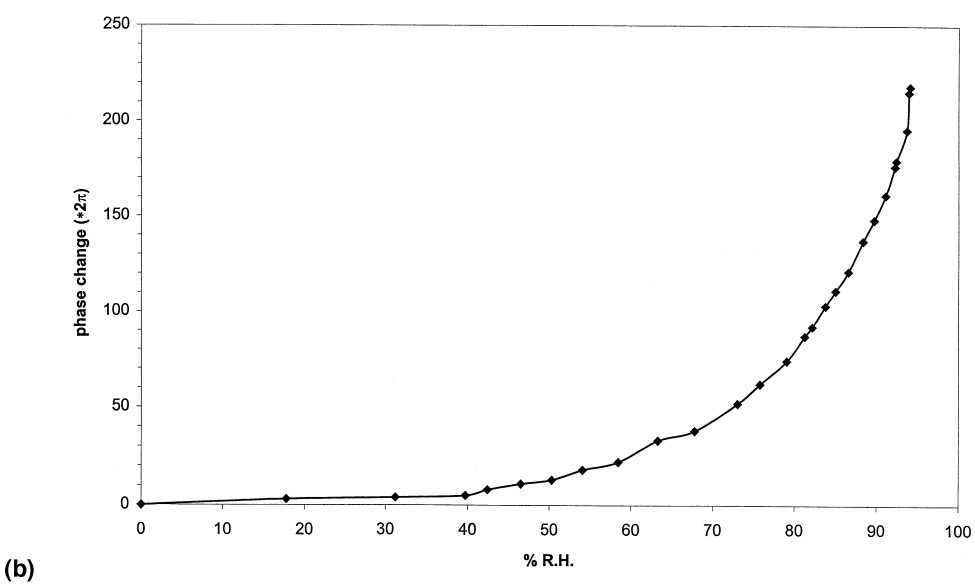

Fig. 22. Preliminary experiments applying a typical sensor for RH measurements: (a) optical output (converted to voltage) without phase modulation as function of time, while increasing the humidity from ~0% to ~15%. (b) The phase change as a function of RH from 0% to ~93%.

type of modulation. The latter makes the read-out signal insensitive to long-term intensity fluctuations due to the light source and/or the fibre-to-chip coupling. This long-term performance of this pigtailed sensor with a sensor window length of 4 mm only, enables a long-term refractive index resolution of $1–3 \times 10^{-7}$.

7.8.4. RH measurement

Fig. 22 refers to a typical MZI sensor provided with gelatine layers in both branches for sensing the RH. Using a two-channel flow-through system, the RH values around both windows can be altered independently of each other. The reference window is kept at constant humidity ($\sim 2\%$, technical nitrogen), while the humidity in the sensing window is varied.

Fig. 22a shows the (non-electro-optically modulated) MZI output, when switching the gas above the sensitive layer from green band nitrogen (water content 10 ppm) to $\sim 15\%$ RH, as measured by a commercial instrument (Rotronic). Remarkable is the very low noise level and the high value of the fringe visibility, being ≥ 0.9. The very smooth interferometer output indicates the absence of TM-polarised light.

Fig. 22b shows the effect if changing the RH from 0% to $\sim 93\%$. The curve depicts the relation between the number of passed fringes, as measured by and displayed on the modulated device. To verify the correctness of the electronic fringe counting using the modulation principle, the experiment has been repeated but now without the modulation, by simply visually counting the number of fringes passed by the non-modulated output signal. In both cases, the number of fringes is identical, being 220. This corresponds to a gelatine refractive index change of ~ 0.094, as calculated from Eq. (9a) inserting there the calculated $\partial N_{\text{eff}}/\partial n_{\text{gelatine}}$-value of 0.36.

8. Prospects

The MZI realised here shows a better short-term phase resolution ($\leq 1 \times 10^{-4} \times 2\pi$) and long-term stability ($\leq 3 \times 10^{-4} \times 2\pi$/h) than those reported in literature [11–20] [21,22]. This mainly stems from the improved chip design and the introduction of an effective modulation principle. These figures can be improved even more by doing the following.

- Increasing the interaction length, now being 4 mm only, to larger values. This however can only be obtained at the cost of the required chip area.
- By taking channels with a width of 2 μm instead of the 4 μm applied now, the lateral contrast can be increased offering the possibility to put both interferometer branches closer together. In that way the temperature differences between both branches will be lowered hence improving the long-term stability.
- Inaccuracies arising from the temperature dependence of the device, especially originating from the sensitive layer, can be reduced whether by thermostating the system or by adjusting the output to the correct value by a software temperature correction. For the latter, an IO thermometer, e.g., an MZI with a large difference between the lengths of the individual branches, has to be added.
- The phase resolution can be further reduced by increasing the oscillator clock rate and by further reducing the electronics noise

If desired, the modulation voltage can be reduced to lower values (at the cost of the required chip area) by increasing the electrode length.

As the used waveguide materials ($Si0_2$, Si_3N_4) allow for a thorough chemical cleaning without damaging the device, it is possible to reuse the sensor chip by repeated removal of the (possibly contaminated) interface layer, followed by applying a fresh or even another type of sensitive layer.

The optical chip can be designed for use at larger wavelengths (~ 850 nm) to enable the use of cheap VCSELs as light source (see Section 7.8). As a consequence, this larger wavelength corresponds to increased $V_{2\pi}$-values and reduced sensitivity, however. Furthermore, due to the small coherence length of VCSELs, the dynamic range of the sensor will be limited.

The device can be used as a stand-alone sensor, but — resulting from the pigtailing — it can also be inserted into a fibre network enabling on-line remote sensing, as desired for example in process technology.

The dimensions of the developed device are not yet minimised. It is expected that the chip dimensions (including the fibre-to-chip couplers) can be reduced to $1 \times 1/2 \times 40$ mm^3, enabling a significant cost reduction.

The used electro-optical phase modulation scheme enables multiplexing of the optical chip. Here, several MZI structures can be used in parallel using one light source only. As also the electrodes can be driven in parallel, only one modulation voltage (feed-back loop) is necessary provided the waveguide uniformity is sufficient. However, each MZI structure requires its individual detection system.

9. Summary

We have demonstrated the design, the fabrication and the testing of an extremely sensitive MZI sensing system, consisting of a laser, an IO chip and processing electronics. The system can be used as a stand alone system but can also be inserted into a fibre network. The system shows a short-term (minutes) phase resolution $\leq 1 \times 10^{-4} \times 2\pi$ and, in a not thermostated room, a long-term (''drift'') stability of $1–3 \times 10^{-4} \times 2\pi$/h. These values are equivalent to a short-term refractive index resolution of $\leq 5 \times 10^{-8}$ an a long-term refractive index stability of

$\sim 1\text{–}2 \times 10^{-7}$. These good resolution characteristics have been obtained by introducing a novel type of phase modulation and individually optimising all components on the chip, connecting them by applying adiabatic transversal tapers.

The design of the system is based on a functional description resulting from (fundamental) MZI sensitivity considerations. The system has been implemented by using low cost SiON technology. The chip contains components for sensing, modulating, splitting, combining, polarising and for efficient fibre-to-chip coupling. The experimentally obtained component characteristics are in good agreement with the design intentions. The system can be modified to further improve the performance.

Acknowledgements

These investigations were supported by the Dutch Innovative Research Program (IOP) Electro-Optics. The authors want to thank Dr.Ir. T.S.J. Lammerink for the realisation of the electronic circuitry, Dr.Ir. T.J. Ikkink for the theoretical signal aspects on the MZI, Ir. B. Middelbos for the work on the electro-optic modulation, Ing. T. Andringa for the fabrication of the optical chips, Ing. R. Wijn for the device and electronics measurements, Ing. A. Hollink, I. Jentink and Ing R. Wijn for the work on the electronics, Dr. H.H.P.Th. Bekman (TNO-FEL) for the deposition of ZnO, Ing. H. Van Wolferen for the photography and B. Otter for the SEM photography.

References

[1] P.V. Lambeck, Integrated opto-chemical sensors, Sensors and Actuators, B: Chemical 8 (1992) 103–116.
[2] O. Parriaux, in: O.S. Wolfbeiss (Ed.), Fibre-Optic Chemical Sensors and Biosensors, Chap. 4, CRC Press, 1991.
[3] W. Lukosz, Principles and sensitivities of integrated optical and surface plasmon sensors for direct affinity sensing and immunosensing, Biosensors and Bioelectronics 6 (1991) 215–225.
[4] R.G. Heideman, R.P.H. Kooyman, J. Greve, Performance of a highly sensitive optical waveguide Mach–Zehnder interferometer immunosensor, Sensors and Actuators, B: Chemical 10 (1993) 209–217.
[5] A. Brandenburg, R. Edelhäuser, F. Hutter, Integrated optical gas sensor using organically modified silicates as sensitive films, Sensors and Actuators, B: Chemical 11 (1993) 361–374.
[6] J. van Gent, Surface plasmon resonance-based chemo-optical sensors, PhD Thesis, University of Twente, 1990.
[7] S. Lofas, B. Johnsson, A novel hydrogel matrix on gold surface plasmon resonance sensors for fast and efficient covalent immobilization of ligans, Journal of the Chemical Society, Chemical Communications (1990) 1526–1528.
[8] B. Liedberg, I. Lundström, E. Steinberg, Principles of biosensing with an extended coupling matrix and surface plasmon resonance, Sensors and Actuators, B: Chemical 11 (1993) 63–72.
[9] K. Tiefentahler, W. Lukosz, Sensitivity of grating couplers as integrated-optical chemical sensors, Journal of the Optical Society of America B: Optical Physics 6 (1989) 209–220.
[10] P.H. Nellen, W. Lukosz, Integrated optical input grating couplers as direct affinity sensors, Biosensors and Bioelectronics 8 (1993) 129–147.
[11] Ch. Stamm, W. Lukosz, Integrated optical difference interferometer as a biochemical sensor, Sensors and Actuators, B: Chemical 18–19 (1994) 183–187.
[12] C. Fattinger, H. Koller, D. Schlatter, P. Wehrli, The difference interferometer: a highly sensitive probe for quantification of molecular surface concentration, Biosensors and Bioelectronics 8 (1993) 99–107.
[13] E.F. Schipper, R.P.H. Kooyman, R.G. Heideman, J. Greve, Feasibility of optical waveguide immunosensors for pesticide detection: physical aspects, Sensors and Actuators, B: Chemical 24–25 (1995) 90–93.
[14] C. Fushen, L. Qu, L. Yungi, X. Yu, Integrated optical interferometer gas sensor, Microwave and Optical Technology Letters 11 (1996) 213–215.
[15] B. Maisenhölder, H.P. Zappe, R.E. Kunz, M. Moser, P. Kiel, Optical refractometry using a monolithically integrated Mach–Zehnder interferometry, Proceedings of IEEE Transducers 1997 (1997) 79–80.
[16] B.J. Luff, S. Wilkinson, J. Piehler, U. Hollenbach, J. Ingenhoff, N. Fabricius, Integrated optical Mach–Zehnder biosensor, Journal of Lightwave Technology 16 (1998) 583–592.
[17] A. Brandenburg, Integrated optical interferometer for refractometry and chemical sensing, Proceedings of SPIE 2783 (1996) 266–276.
[18] R.G. Heideman, G.J. Veldhuis, E.W.H. Jager, P.V. Lambeck, Fabrication and packaging of integrated chemo-optical sensors, Sensors and Actuators, B: Chemical 35–56 (1996) 234–240.
[19] P.V. Lambeck, R.G. Heideman, T.J. Ikkink, Phasemodulated Mach–Zehnder interferometer for sensor applications, Medical and Biological Engineering and Computing 34 (Suppl. 1) (1996) 145–148, Part 1.
[20] F. Brosinger, H. Freimuth, M. Lacher, W. Ehrfeld, A label-free affinity sensor with compensation of unspecific protein interaction by a highly sensitive optical Mach–Zehnder interferometer on silicon, Sensors and Actuators, B: Chemical 44 (1997) 350–358.
[21] B. Maisenhölder, H.P. Zappe, R.E. Kunz, P. Riel, M. Moser, J. Edlinger, A GaAs/AlGaAs-based refractometer platform for integrated optical sensing applications, Sensors and Actuators, B: Chemical 38–39 (1997) 324–329.
[22] E.F. Schipper, Waveguide immunosensing of small molecules, PhD Thesis, University of Twente, 1997.
[23] T.J. Ikkink, Interferometric interrogation concepts for integrated electro-optical sensor systems, PhD Thesis, University of Twente, 1998.
[24] T.M. Koster, P.V. Lambeck, Realisation and characterisation of a fabrication tolerant passive polarisation converter in SiON technology, Proceedings of 1998 IEEE/LEOS Symposium, Gent, Belgium (1998) 117–120.
[25] C. Polhemus, Two-wavelength interferometry, Applied Optical Letters 12 (1973) 2071–2074.
[26] K. Wörhoff, Optimised LPCVD SiO_xN_y-waveguides covered with calixarene for non-critically phase-matched second harmonic generation, PhD Thesis, University of Twente, 1996.
[27] C. Jones, K. Cooper, M. Nield, R. Waller, J. Rush, J. Collins, P. Fiddyment, I. Lealman, Hybrid integration using silica-on-silicon optical motherboards, Proceedings of IPR 1996 (1996) 604–607.
[28] R. Moosburger, B. Schüppert, U. Fisher, K. Petermann, Passive alignment technique for all-silicon integrated optics, Proceedings of Integrated Photonics Research 1996, Boston, USA, April 29–May 2 (1996) 565–568.
[29] G.E. Henein, J.V. Gates, L.J. Mulligan, H.M. Presby, J.F. de Jong, Fibre to laser coupling on silicon optical bench platform, Proceedings of Integrated Photonics Research 1996, Boston, USA, April 29–May 2 (1996) 396–399.
[30] O.G. Ramer, Single-mode fibre-to-channel waveguide coupling, Journal of Optical Communications 2 (1981) 122–127.
[31] R.G. Heideman, P.V. Lambeck, Integrated optical sensor system for

detection of chemical concentrations, Proceedings of 1997 IEEE/LEOS Symposium, Eindhoven (1997) 29–32.
[32] R.G. Heideman, P.V. Lambeck, Simple and reusable fibre-to-chip interconnect with adjustable coupling efficiency, Proceedings of SPIE 3099 (1997) 238–247, Micro-Optical Technologies for Measurement, Sensors, and Microsystems II and Optical Fibre Sensor Technologies and Applications, Munich, Germany.
[33] H.H.P.Th. Bekman, K.W. Benoit, J.L.L. Joppe, Post-deposition annealing of RF-sputtered zinc-oxide films, Applied Surface Science 70/71 (1992) 347–350.
[34] R.G. Heideman, P.V. Lambeck, J.G.E. Gardeniers, High quality ZnO layers with adjustable refractive indices for integrated optics applications, Optical Materials 4 (1995) 741–755.
[35] F.C.M. van de Pol, A pump based on micro-mechanical techniques, PhD Thesis, University of Twente, 1989.
[36] Handbook of Chemistry and Physics, 78th edn., CRC Press, New York, 1997–1998.
[37] M.J. Vellekoop, C.C.G. Visser, P.M. Sarro, A. Venema, Compatibility of zinc oxide with silicon IC processing, Sensors and Actuators A21–A23 (1990) 1027–1030.
[38] B.B.V. Software, The Netherlands.
[39] O. Parriaux, G.J. Veldhuis, Normalised analysis for the sensitivity optimisation of integrated optical evanescent wave sensors, Journal of Lightwave Technology 16 (1998) 573–582.
[40] A. Yariv, P. Yeh, Optical Waves in Crystals, Chap. 7, Wiley, 1983.
[41] R. Alferness, Waveguide electro-optic modulators, IEEE Transactions on Microwave Theory and Techniques MTT-30 (1982) 1121–1137.
[42] O.J. Glembochi, R.E. Stahlbush, Bias-dependent etching of silicon in aqueous KOH, Journal of Electrochemical Society 132 (1985) 145–158.
[43] E.C.M. Pennings, Bends in optical ridge waveguides, modelling and experiments, PhD Thesis, University of Delft, 1990.
[44] H. Yanagawa, T. Shimizu, S. Nakamure, I. Ohyama, Index- and dimensional taper and its application to photonic devices, IEEE Journal of Lightwave Technology 10 (1992) 587–591.
[45] G.I. Parishi, S.E. Haszko, G.A. Rozgonyi, Tapered windows in SiO_2: the effect of NH_4F:HF dilution and etching temperature, Journal of Electrochemical Society: Solid State Science and Technology 124 (1977) 917–921.
[46] LEE, The Netherlands.

René G. Heideman (1965) obtained his PhD in Applied Physics at the University of Twente in 1993. At the same University, he worked for several years as post-doc. His research areas were the development of new photonic devices and bio-chemical sensors. In 1997, he joined Twente MircoProducts as product specialist on IO-MST devices. Currently, he works at Mierij Meteo as head of the R&D-Integrated Optics section.

Paul V. Lambeck (1939) is an associate professor of Materials Science at the University of Twente, The Netherlands. He is one out of two groupleaders in the Lightwave Device Group of the MESA Institute of this University. His research areas are integrated optical devices and photonic circuits for application in the optical telecommunication and sensors. At present, his research focuses on integrated optical switches, amplifiers. MOEMS and chemo-optical sensors.